Kinematic modelling of large tremors in the Groningen field using extended seismic sources

First results related to the Zeerijp tremor M_L 3.4

Shell Global Solutions

H.M. Wentinck

Datum August 2018

Editors Jan van Elk, & Dirk Doornhof

General Introduction

The Huizinge earthquake of 16th August 2012 with a magnitude of M_L = 3.6 had a profound impact on the Groningen community and led to the acceleration of the research program into induced seismicity in Groningen. As part of this program new capabilities were developed. For instance, geomechanical modelling of rupture processes taking place in the depleted gas reservoir of the Rotliegend formation was improved.

Using these capabilities, the Huizinge earthquake of 2012 was revisited (Ref. 1 and 2). In this report the same techniques are used to study the more recent Zeerijp (M_L = 3.4) earthquake of 8th January 2018 (Ref. 3). Since the Huizinge earthquake the network of geophones and accelerometers installed in the Groningen field has been significantly expanded. For the Zeerijp earthquake much more recordings are therefore available than for the Huizinge earthquake. Furthermore, methods to image the faults in the area and to estimate the earthquake hypocenters have also been further developed. This allows the fault hosting this earthquake to be determined with more precision.

References

1. Kinematic modelling of large tremors in the Groningen field using extended seismic sources – Part 1, H.M. Wentinck, August 2017
2. Kinematic modelling of large tremors in the Groningen field using extended seismic sources – Part 2, H.M. Wentinck, July 2018
3. Special Report on the Zeerijp Earthquake – 8th January 2018, NAM, Taco den Bezemer and Jan van Elk.

Title	**Kinematic modelling of large tremors in the Groningen field using extended seismic sources First results related to the Zeerijp tremor ML 3.4**	**Date**	August 2018
		Initiator	NAM
Author(s)	H.M. Wentinck	**Editor**	Jan van Elk and Dirk Doornhof
Organisation	Shell Global Solutions	**Organisation**	NAM
Place in the Study and Data Acquisition Plan	Study Theme: Geomechanical Modelling Comment: The Huizinge earthquake of 16th August 2012 with a magnitude of M_L = 3.6 had a profound impact on the Groningen community and led to the acceleration of the research program into induced seismicity in Groningen. As part of this program new capabilities were developed. For instance, geomechanical modelling of rupture processes taking place in the depleted gas reservoir of the Rotliegend formation was improved. Using these capabilities, the Huizinge earthquake of 2012 was revisited (Ref. 1 and 2). In this report the same techniques are used to study the more recent Zeerijp (M_L = 3.4) earthquake of 8th January 2018 (Ref. 3). Since the Huizinge earthquake the network of geophones and accelerometers installed in the Groningen field has been significantly expanded. For the Zeerijp earthquake much more recordings are therefore available than for the Huizinge earthquake. Furthermore, methods to image the faults in the area and to estimate the earthquake hypocenters have also been further developed. This allows the fault hosting this earthquake to be determined with more precision.		
Directly linked research	1. Reservoir engineering studies in the pressure depletion for different production scenarios. 2. Seismic monitoring activities; both the extension of the geophone network and the installation on geophones in deep wells. 3. Geomechanical studies 4. Subsidence and compaction studies.		
Used data	KNMI Earthquake catalogue Geological maps of faults in the Rotliegend reservoir		
Associated organisation	Shell Global Solutions		
Assurance			

report for NAM 2018

Kinematic modelling of large tremors in the Groningen field using extended seismic sources

first results related to the Zeerijp tremor M_L 3.4

by

H.M. Wentinck

Executive Summary

This work is about the kinematic modelling of the relatively large Zeerijp M_L 3.4 tremor of January 8 2018 in the Groningen field. The model uses an extended seismic source which is represented by a series of double couples along fault strike on the rupture plane. The model includes the geometry of the geological subsurface formations and a seismic velocity model for these formations. The hypocentre and focal mechanism of the seismic source model are based on the results of seismic moment tensor inversion done by others.

The simulated displacements for several seismometer stations near the tremor epicentre correspond fairly well with the observed ones. But for a few stations, the observed displacements are considerably smaller than the simulated ones. A variation of the seismic source parameters does not lead to a significant improvement in this respect and, so far, the origin of this discrepancy is not clear.

This report includes also the spectra of the observed displacements, the so-called corner frequencies derived from it and the apparent source time functions for the M_L 3.4 tremor. The latter could be derived using the technique of empirical Green functions (EGFs) and comparing the M_L 3.4 tremor displacements with displacements following from a similar but smaller M_L 1.7 tremor at about the same tremor hypocentre.

The variation in the apparent source time functions with the receiver-tremor azimuth angle indicates that the rupture has propagated along fault strike in the north-west direction rather than along fault dip. This preliminary observation has not been used in this work to constrain the extended seismic source model in the simulations.

Table of Contents

Table 0.1 : List of frequently used symbols

Symbol	Property	Unit
....	....	....
$\boldsymbol{a}$	displacement acceleration vector	m/s^2
D	relative displacement or slip over a slip plane	m
D	damping or isotropic loss factor for attenuation of seismic waves	-
f	frequency	Hz
f_c	corner frequency of the ground motions	Hz
$f(t)$	source time function	-
f	magnitude of a point force	N
$\boldsymbol{f}$	force vector	N
i	take off angle of ray	degree/radian
l_{DC}	arm of the double couple	m
L	length of rupture plane along fault strike	m
M	moment magnitude	Richter
M_L	local magnitude	Richter
$\boldsymbol{m}$	moment tensor defining the slip plane orientation and slip direction	-
$\boldsymbol{M}$	moment tensor	Nm
M_0	seismic moment	Nm
n	shape parameter of modified source time function	-
$\boldsymbol{n}$	unit vector normal to the slip plane	-
Q	quality factor for the attenuation of seismic waves	m
Q	quotient of spectra $F[u_L(t)]/F[u_S(t)]$	-
r	distance between tremor epicentre and receiver	m
R	radius of circular rupture plane	m
S	surface area of rupture plane	m^2
t	time	s
t_{onset}	onset time of source time function	s
t_r	rise time of source time function	s
t_R	duration of the rupture in the slip plane	s
$t_{trigger}$	trigger time of a point force of an extended source	s
Δt_{ps}	time difference between the arrivals of primary and secondary waves	s
$\boldsymbol{u}$	displacement vector	m
V_p	velocity of primary wave	m/s
V_s	velocity of secondary wave	m/s
V_r	rupture velocity	m/s
$V_{r,strike}$	rupture velocity along fault strike	m/s
$\boldsymbol{v}$	displacement velocity vector	m/s
W	width of rupture plane along fault dip	m
$\boldsymbol{x}$	Cartesian coordinates of the receiver (or location in the field)	m
x, y, z	coordinates used for analytical expressions	m
X, Y, Z	coordinates based on the Dutch Rijksdriehoeksstelsel	m

Table 0.2 : List of frequently used symbols, continued

Symbol	Property	Unit
δ	dip angle of fault	degree/radian
δ_{ij}	Kronecker delta function	-
$\Delta\tau$	breakdown stress drop over fault plane during rupture	Pa
Δt_{50}	period in source time function exceeds 50% of the maximum value	s
Δt_{PS}	time difference between arrivals of P and S waves	s
ζ	damping or isotropic loss factor for the attenuation of seismic waves	-
$\boldsymbol{\zeta}$	Cartesian coordinates of the source	m
θ	angle between fault strike and line between source and receiver	degree/radian
λ	wavelength	m
λ	rake angle of slip vector	degree/radian
ρ	mass density of rock	kg/m^3
τ	time	s
ϕ	fault strike azimuth angle	degree/radian
ϕ_s	source-receiver azimuth angle	degree/radian
ω	angular or circular frequency of a wave	radian/s

Table 0.3 : List of frequently used symbols, continued

Symbol	Refers to
....	....
subscripts	
area	selected region or area
app	apparent source time function
arr	arrival time of wave at receiver
DC	double couple
hor	horizontal component of displacement, velocity or acceleration
p	primary or compressive wave
rad	radial component of displacement, velocity or acceleration
rec	receiver
rms	root mean square value
s	secondary or shear wave
strike	along fault strike
tra	transverse component of displacement, velocity or acceleration
ver	vertical component of displacement, velocity or acceleration
abbreviations	
EBN	Energie Beheer Nederland
EGF	empirical Green function
FEM	finite element method
KNMI	Koninklijk Nederlands Metereologisch Instituut
NAM	Nederlandse Aardolie Maatschappij
P	primary wave
RD	Dutch Rijksdriehoeksstelsel coordinate system
S	secondary wave
SH	secondary horizontal wave
SV	secondary vertical wave

Chapter 1

Introduction

This work is part of an ongoing effort to understand tremors in the Groningen field, their ground motions and effects on buildings[1]. Currently, the hypocentre and focal mechanism of seismic sources in the Groningen field are accurately and quickly determined by KNMI, SGS-I and ExxonMobil from ground displacements recordings by the extensive seismometer network in this field. This is done on a regular basis for tremors with $\mathrm{M_L} > 1.4$ using seismic moment tensor inversion methods and in combination with full wave form simulations or other models and using an accurate velocity model of the subsurface[2].
It is found that the vast majority of the seismic sources are located in the reservoir. The accuracy of the location of the epicentre is 100 - 200 m, which allows us to map the source on one of the many faults in the Groningen field. In most cases, the moment tensor primarily contains double couple components which are related to slip along a fault plane with the slip direction of the hanging wall largely downwards along fault dip[3].

This work is about the Zeerijp tremor from January 8 in 2018 with a local magnitude $\mathrm{M_L}$ 3.4. In the same region of the Groningen field, two other large tremors have occurred in the past. These are the Westeremden $\mathrm{M_L}$ 3.5 tremor in 2006 and the Huizinge $\mathrm{M_L}$ 3.4 tremor in 2012. Compared to these two tremors, the Zeerijp tremor has been recorded by much more seismometers. The network of seismometer stations operated by KNMI has

---

[1] Recent results can be found in reports and presentations of NAM (2015), Stafleu et al. (2016), Bommer et al. (2015), Edwards et al. (2016), Bommer (2016), Burnett (2016) and van Dedem (2016) in relation to ground motion prediction equations (GMPE's), and of Dost and Kraaijpoel (2013), Dost (2016), Burnett (2016), Terrell (2016) and Lawrence et al. (2015) in relation to seismic moment tensor solutions of large tremors and in relation to the interpretation of tremors recorded by the downhole geophones in the Zeerijp and Stedum wells in the Groningen field.

[2] Often, the focal mechanism of a seismic source can be described by the azimuth and dip angles of the slip plane and the slip direction (or so-called rake angle). When the subsurface has various formations with different wave velocities, advanced calculations are needed to obtain the seismic source parameters from the ground displacements. When the formations are flat around the tremor hypocentre, software for seismology, such as "Cake" from pyrocko.org GFZ-Potsdam (F.R.G.) can be used. This software is used by KNMI. Otherwise, full wave propagation simulations based on finite difference methods are integrated into the inversion methods. This is done by ExxonMobil and SGS-I.

[3] These results originate from KNMI and SGS-I and will be reported in the near future.

been significantly expanded over the last five years. Furthermore, the orientation of the accelerometers on the ground and the geophones in the shallow boreholes at 50 - 200 m depth of almost all stations have been determined in a collaborative effort by KNMI and SGS-I using calibration shots and very large earthquakes from other continents. Taking advantage of all recorded motions, the location of the hypocentre and the focal mechanism (or moment tensor) of the source of the Zeerijp tremor have been accurately derived by KNMI and SGS-I, see Chapter 2.
Using this data, we have simulated the Zeerijp tremor with a similar kinematic model as was developed for the Huizinge tremor in 2012, see Wentinck (2017) and Wentinck (2018b). The aim of this work is to check whether the ground motions from the kinematic modelling are consistent with the observed ones and whether the dimensions of the rupture plane could be determined from the motions recorded by most of the nearby B stations with a limitation that the information that can be used is contained in wave frequencies below 5 Hz. If ground displacements are sufficiently close to the hypocentre of a relatively large tremor of $\mathrm{M_L} > 3$, these displacements may contain information about the rupture plane dimensions.

We found for several stations a reasonable correspondence between the observed and simulated displacements. However, the correspondence is less for at least two stations. The use of somewhat other source parameters did not significantly reduce the present differences between the simulated and observed signals. Regarding these differences it is hard to say more about the rupture plane dimensions.

Chapter 2 presents the field data used and the set-up of the FEM simulations. Chapter 3 shows the results. A short discussion follows in Chapter 4. More field data is given in Appendix A. Appendix B gives seismometer data of the Zeerijp $\mathrm{M_L}$ 3.4 tremor including spectra, corner frequencies and apparent source time functions. Appendix C shows additional simulation results. Appendix D gives details about the implementation of the seismic source in the simulations and some relations between corner frequencies and slip plane dimensions.

Chapter 2

Field data used

2.1 Subsurface geometry

According to Dost et al. (2018), the moment magnitude M [Richter] is about equal to the local magnitude $\mathrm{M_L}$ [Richter] for $M > 2.5$. Using $\mathrm{M_L} = M \sim 3.4$ and Kanamori's relation between seismic moment M_0 [J] and moment magnitude M, i.e., $\log M_0 = 3/2(M + 6.07)$, the corresponding seismic moment M_0 of the simulated tremor is $M_0 = 160$ TJ. According to seismic moment tensor inversions by Bernard Dost (KNMI) and Ewoud van Dedem (SGS-I), the tremor epicentre coordinates of the Zeerijp $\mathrm{M_L}$ 3.4 tremor are X = 245714 m and Y = 597574 m and X = 245600 m and Y = 597600 m, respectively[1]. The differences in the coordinates are within the accuracy of methods used. The tremor hypocentre or the centre of the seismic source is in the reservoir at a depth of about 2950 m.

Figure 2.1 shows a map of the faults around the epicentre of the Zeerijp $\mathrm{M_L}$ 3.4 and $\mathrm{M_L}$ 1.7 tremors and the locations of the seismometer stations used. The faults shown are from the NAM fault database, primarily used for reservoir flow modelling and geomechanical calculations.

The hypocentre of the Zeerijp tremor is on a minor fault mFS7-Fault-54 in the reservoir. According to the NAM fault database for reservoir modelling and geomechanics, the fault strike azimuth and fault dip angles of the mFS7-Fault-54 fault near the tremor hypocentre are $\phi \sim 315 \pm 10^\circ$ and $\delta \sim 80 \pm 3^\circ$, respectively[2]. The fault throw near the tremor hypocentre is about 40 m which is relatively small compared to the reservoir thickness of about 270 m. The fault strike azimuth corresponds quite well with the one derived from seismic moment tensor inversions by Bernard Dost (KNMI) and Ewoud van Dedem (SGS-I). The fault is dipping to the east.

The correspondence is less good for the dip angle of the fault δ. Bernard Dost (KNMI)

---

[1] X and Y are coordinates of the Dutch Rijksdriehoeksstelsel coordinate system.

[2] The fault strike azimuth angle ϕ is defined as the angle between the Earth north direction and the fault strike where it is measured clockwise round from north.

and Ewoud van Dedem (SGS-I) derive $\delta \sim 67°$. On the other hand, Alan Wood (SGS-I) derives from ant-tracking, a dip angle in the range 75 - 80° in agreement with the NAM fault database, see Figure 2.3 . Around the tremor hypocentre, the fault is quite smooth along dip but less smooth along fault strike.
According to ant-tracking results of Marloes Kortekaas (EBN), the structure of fault mFS7-Fault-54 around the Zeerijp tremor hypocentre seems more complicated, see Figures 2.2 and 2.3 . A reverse and a normal fault join around the tremor hypocentre. The ant-tracking of the fault is clear at top of the reservoir but becomes in the reservoir less clear. The broken fault on the right side dips to the east. Regarding the results of the seismic moment tensor inversion, we disregard in this report slip on the reverse fault at the left side.

The wave velocities in the subsurface formations around the tremor epicentre have been calculated from the rock density ρ [kg/m^3] and the primary (P) and secondary (S) wave velocities V_p and V_s [m/s]. They originate from NAM's seismic velocity model which has been updated in 2015 and is also used in Wentinck (2017) and Wentinck (2018b)[3].

---

[3] The NAM seismic velocity model has been provided by Remco Romijn (NAM) in the form of Excel and .csv files.

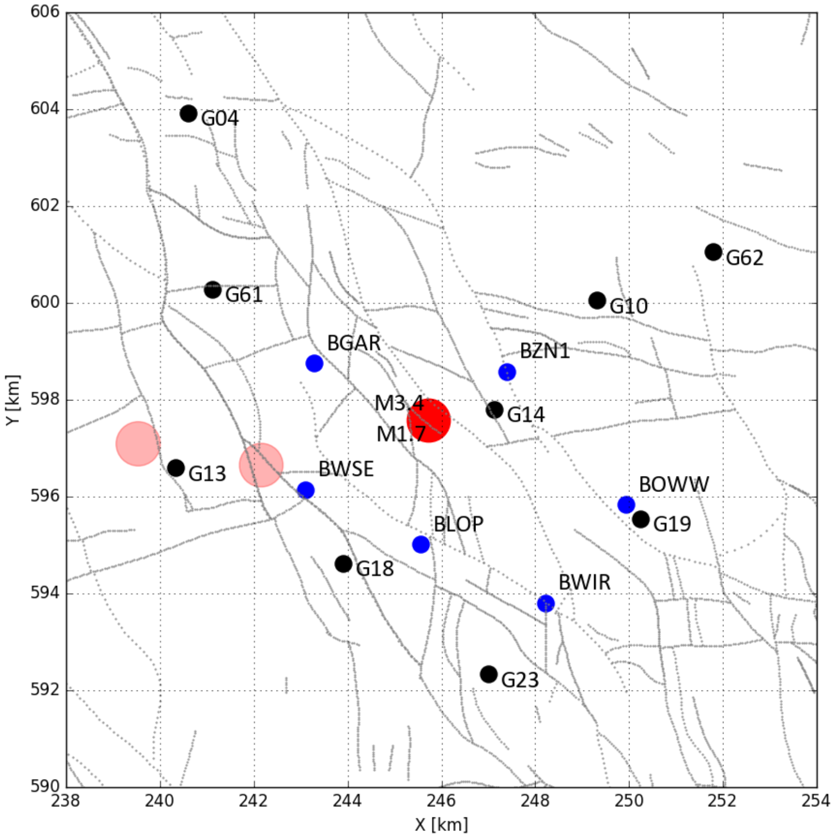

Figure 2.1 : Faults and locations of the epicentre of the Zeerijp M_L 3.4 tremor and the seismometer stations used.

The thin grey dotted and solid lines are intersections of the faults with the top horizon of the Rotliegend reservoir according to the NAM fault database. This database is primarily used for reservoir flow models and for geomechanical calculations.

The red dot shows the location of the M_L 3.4 tremor. The two pink dots show the epicentres of the Huizinge 2012 M_L 3.4 (left) and Westeremden 2006 M_L 3.5 (centre) tremors. The blue and black dots show the B stations with the ground accelerometers and the G stations with ground accelerometers and shallow boreholes with 4 geophones at 50, 100, 150 and 200 m depth, respectively. All stations are operated by KNMI.

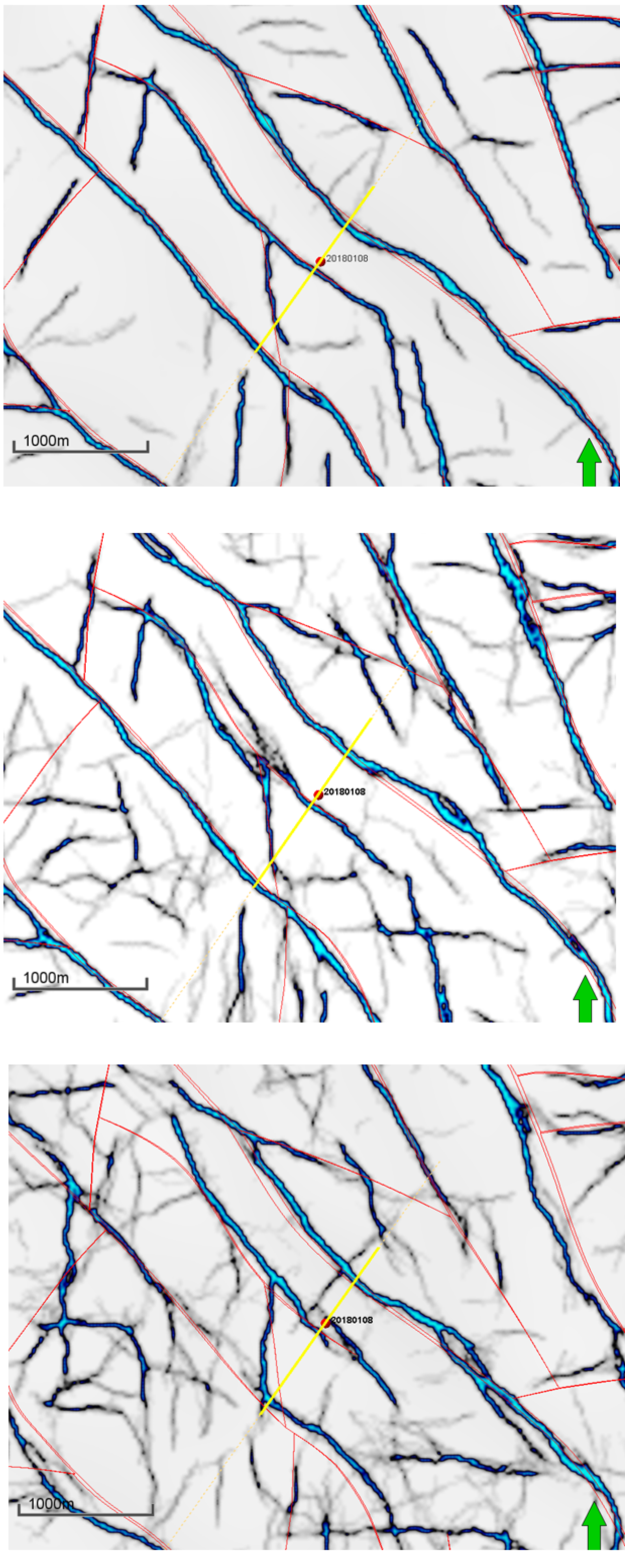

Figure 2.2 : Faults derived from ant-tracking faults using Petrel$^{\text{TM}}$ on the seismic data cube of 2015 of the Groningen field by Marloes Kortekaas (EBN). From top to bottom, the figures show planes at the depth of the top of the reservoir, at the depth of the tremor hypocentre and at the depth of the bottom of the reservoir, respectively. Near the tremor hypocentre there may be a fault jog, i.e., an overstep or a bend that connects two sub-parallel but non-collinear portions of a fault zone.
The red dot shows the tremor hypocentre with RD coordinates X = 245714 m, Y = 597574 m and Z = -2950 m. The thin red lines show faults according to the NAM fault database.

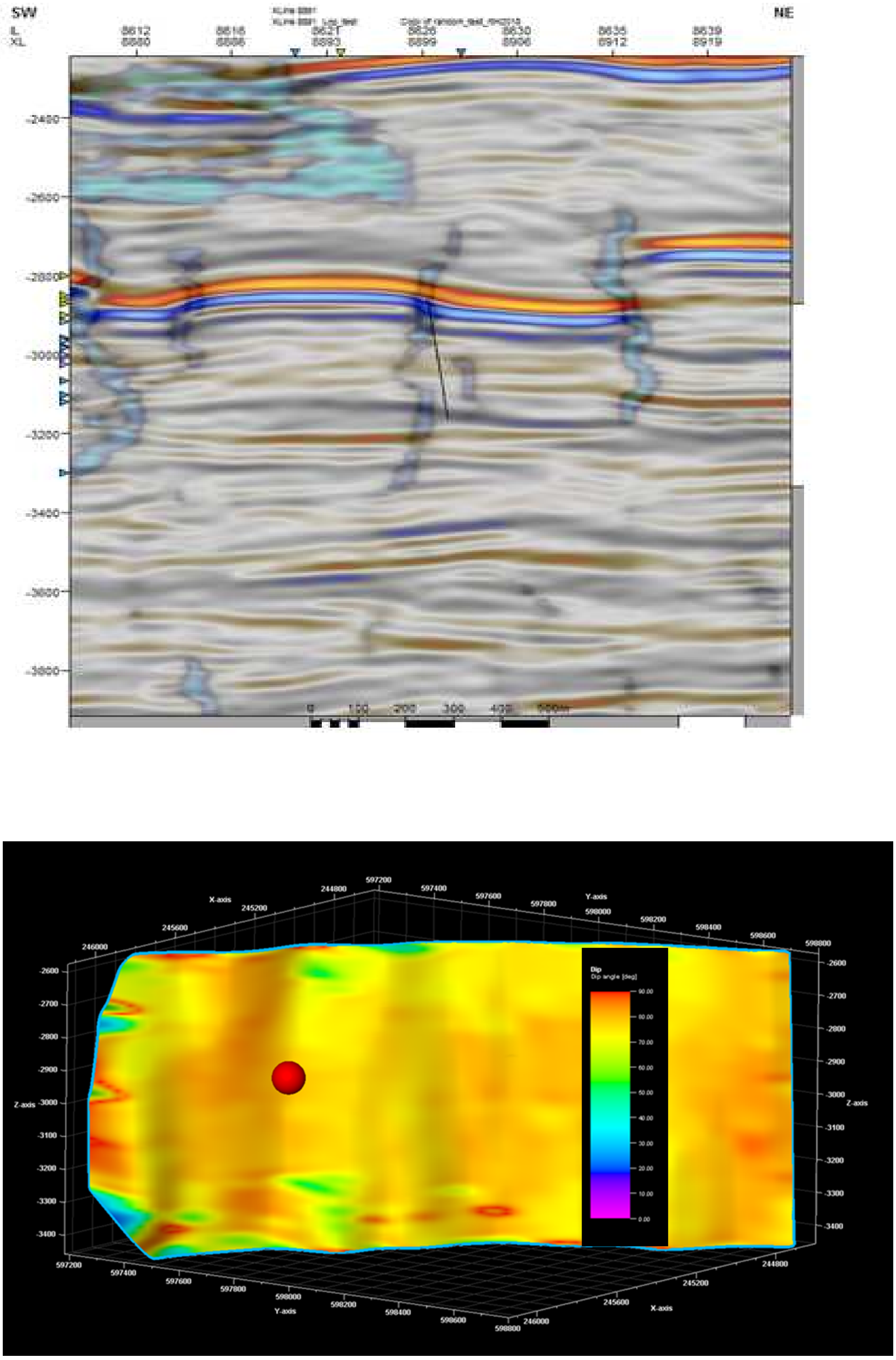

Figure 2.3 : Part of the mFS7-Fault-54 fault from ant-tracking. The top figure is from Marloes Kortekaas (EBN). Without vertical exaggeration, it shows a cross-section of the subsurface along the yellow line shown in Figure 2.2 . The normal broken fault on the right has a dip angle which compares well with the dip angle derived by Alan Wood (SGS-I). The thin black line shows the fault according to the NAM fault database.
The bottom figure is from Alan Wood. About 40% of the fault plane has a dip angle between 76 and 80° and about 98% of the fault plane has a dip angle between 72 and 84°.

2.2 Set up of finite element method simulations

The simulated tremor has a seismic moment $M_0 = 160$ TJ and hypocentre coordinates X = 245714 m, Y = 597574 m and Z = -2950 m. Using the NAM subsurface seismic velocity model 2015, the following subsurface formations have been simplified as this work is focussed on the low frequency content of the body waves which reach ground accelerometers within a distance of 8 km from the tremor epicentre. From top to bottom:

- The shallow subsurface, i.e. the sand, clay and peat layers within 100 m below the surface. Primarily, the shear modulus of these sediments is small compared to the one of the deeper rock. It leads to a significantly lower S wave velocity and a relatively strong attenuation of S waves in the shallow subsurface. The combined effect is a ground motion amplification of the S waves of about a factor 2, in agreement with Dost et al. (2004), a delay of the S wave arrivals at the ground accelerometers of about 0.2 - 0.3 s and some bending of the S wave vertically upwards. This amplification adds to the usual amplification of subsurface waves when reaching the free surface[4].
  In the simulations, we do not include an explicit detailed velocity model for the slow down of the S wave in the shallow subsurface. Since the S wave primarily manifests itself in the radial and transverse components of the displacements, we multiply the simulated horizontal components with a factor 2 to account for the amplification of the S wave in the shallow subsurface. The P wave, which manifests itself primarily in the vertical component, hardly slows down in the shallow subsurface and is not amplified. We assume that the vertical ground displacements during the passage of the P wave are in this respect quite well modelled.

- The Brussel Sandstone member in the lower North Sea formation is disregarded. Incorporating this relatively hard sandstone would lead to lower travel times through the North Sea formation than would follow from the velocity model used and would lead to some scattering of high frequency waves passing through it[5]. The thickness of this layer is less than 200 m but. It is poorly mapped but it is believed that it substantially varies over the field.

- The Triassic, Altena and Rijnland formations have been grouped to form a single subsurface formation. The P and S velocities in this formation are weighted means of the velocities in the three formations[6].

- The floater and anhydrite layers which are part of the Zechstein salt above the reservoir have a constant thickness to solve meshing problems.

---

[4] In the FEM simulations, the amplification of waves reaching the surface is automatically calculated using the appropriate boundary condition at the surface.

[5] According to check shots with explosives in the field significantly lower travel times to the surface are observed than modelled for direct P waves between 4 - 7 km from the epicentre, see Langemeijer (2017), Figure 28. The author suggests that this may be due to presence of this sandstone.

[6] The weighting ensures that the travel times of vertical P and S waves in the combined formation are equal to the travel times of these waves through the three stacked formations.

- The late Carboniferous and the formations below the late Carboniferous are assumed to be uniform over the region of interest. The velocity profile as a function of depth in these formations is assumed to be typical and wave reflections from below the base of the reservoir are ignored[7].

The domain of wave propagation in the FEM simulations covers the region of about 10 ×10 km around the tremor epicentrea and a depth of 6 km. The maximum mesh sizes used are 50 m for the upper North Sea formation, the floater and anhydrite layer, 65 m for the Lower North Sea formation, 85 m for the Chalk and upper Zechstein formation and combined Trias, Altena and Rijnland formation and 80 m for the reservoir. Waves which propagate into the Carboniferous are not reflected at the horizon between the Dinantium and Carboniferous below it. These mesh sizes limit the frequency bandwidth of useful information in the simulated signals as they sometimes lead to artificial oscillations at frequencies above a few Hertz. So, we can only compare the prominent low frequency features in the observed and simulated displacements.

The seismic source is similar as the one used in Wentinck (2017). The slip or rupture plane has been divided in a number of relatively small slip patches along fault strike. Each slip patch has two double couples and a source time function. The source time functions, which define the slip rate for each slip patch, are all the same except for a time shift. The time shift is determined by the rupture velocity along fault strike and the location of the slip patch with respect to the tremor hypocentre[8].

---

[7] The pre- or sub-Permian formations below the reservoir are not uniform over the Groningen field. During the Namurian period in the late Carboniferous, mainly basin facies, such as shales, mudstones and peat, were deposited in the Groningen area. During the later Westphalian period in the late Carboniferous, a deltaic river system progrades from the south-east depositing more sandy sediments and non-uniformly filling valleys in a fluvial area. These sediments directly subcrop the Rotliegend sandstone in the Groningen field. According to the so-called Dutch Velmod-2 project, the P wave velocity in the top of the Namurian gradually varies over the Groningen field, see for example Langemeijer (2017), Figure 22 for the north-east Netherlands.
Significant wave reflections can be expected from the horizon between the Dinantium and Namurian (or between the early and late Carboniferous) formations at more than 6 km depth in the Zeerijp region. Such waves travel at least 6 km through the Namurian formation before they pass again the horizon between the late Carboniferous and Rotliegend formations while moving upwards. For typical mean P and S wave velocities in the Namurian of about 5 and 3 km/s, the reflected P and S waves arrive at the surface at least 1.2 and 2 s after the corresponding direct body waves in the region of interest.
Also, the late Devonian carbonates and early Carboniferous (or Dinantium, Mississippian or Visean) carbonate limestones at varying depth over the field but deep below the reservoir guide and redirect downwards propagating (or diving) waves back to the surface because waves in these rocks have propagate faster than in the overlying late Carboniferous (Pennsylvanian) siliclastics (or sandstones/shales). According to one-dimensional ray tracing models and two-dimensional full wave propagation finite difference models, such waves appear first at the surface at a distance of more than 10 km away from the epicentre, see for example Spetzler and Dost (2017) and Langemeijer (2017). For the Huizinge tremor and the stations of interest, these so-called diving waves hardly interfere with the direct body waves when reaching the surface.

[8] The rupture velocity is the velocity with which the rupture front propagates over the slip plane. The source time function completely defines the slip rate or the dynamics of the rupture process in the

The modified source time functions used for each slip patch have shape parameters $\tau_r = 0.08$ s, $n = 2$. For these parameters, the time in which the rupture would propagate along fault dip is about 0.15 s. This time is sufficient to propagate a rupture over a depth of about 0.3 km in one direction for a rupture velocity $V_r = 2$ km/s. For convenience, the main features of the source time functions used are given in Appendix D.

The duration of rupture propagation along fault dip and the duration of rupture propagation along fault strike are of the same order as the mean duration of the rupture as derived from the observed displacements, see Appendix B. So far, we have not used the observed displacement spectra of various stations and the apparent source time functions (using empirical Green functions anddisplacements of a smaller but similar tremor) to constrain the extended source model in another way. The interpretation of the spectra needs more study.

---

patch. For a point source, the dimensions of the slip plane, the slip rate and the rupture velocity are indistinguishably included in the time dependence of a single source time function.

Chapter 3

Results

Figure 3.1 shows the observed displacements recorded by the ground accelerometers of 11 B and G stations[1] and the corresponding simulated displacements.
The radial and transverse displacements have been calculated using the locations of the tremor epicentre and the stations and the orientations of the geophones and accelerometers in the horizontal plane[2]. The station locations and geophone and accelerometer orientations used are given in Appendix A, Table A.4 .

Figures 3.1 and 3.2 show the observed and simulated displacements of the accelerometers at the surface. The simulated ones have been filtered with the same 0.2 Hz 2^{nd} order high pass filter similar as the displacements recorded by the ground accelerometers. In addition, the simulated radial and transverse displacements have been shifted 0.2 s in time and have been amplified twice to include the typical effect of the slow down of the S wave in the shallow subsurface. The correspondence is reasonable considering that the amplification factor for the S waves vary with the locations of the stations and the accuracy of the observed tremor moment magnitude is ± 0.1 Richter.
Still, the simulated amplitudes for stations G14, G18, BLOP and BWIR are significantly larger than observed. This also holds for the geophones of stations G14 and G18. So far, we don't have a good explanation for this. Variation of the source parameters does not significantly improve the comparison between simulation and observation. Also, another slip direction or rake angle has no beneficial effect in this respect.

In Appendix B, §B.4, the observed time difference of the observed and simulated arrival times of the P and S waves Δt_{PS} [s] are plotted against the distance of the stations from the tremor epicentre. The simulated arrival times of the P and S waves correspond

---

[1] The simulated displacements of the other 4 stations on the map in Figure 2.1 are too close to the boundary of the domain for simulation to be useful. Although low-reflecting boundaries have been applied to the side walls of the domain, part of the energy of the surface waves on the free surface still reflects back into the domain.

[2] The orientations of the ground accelerometers and the geophones in the shallow boreholes at 50 - 200 m depth of almost all stations have been determined in a collaborative effort by KNMI and SGS-I using calibration shots and very large earthquakes from other continents.

fairly well with the observed ones and results from ray tracing calculations for a point source using 5 subsurface formations.

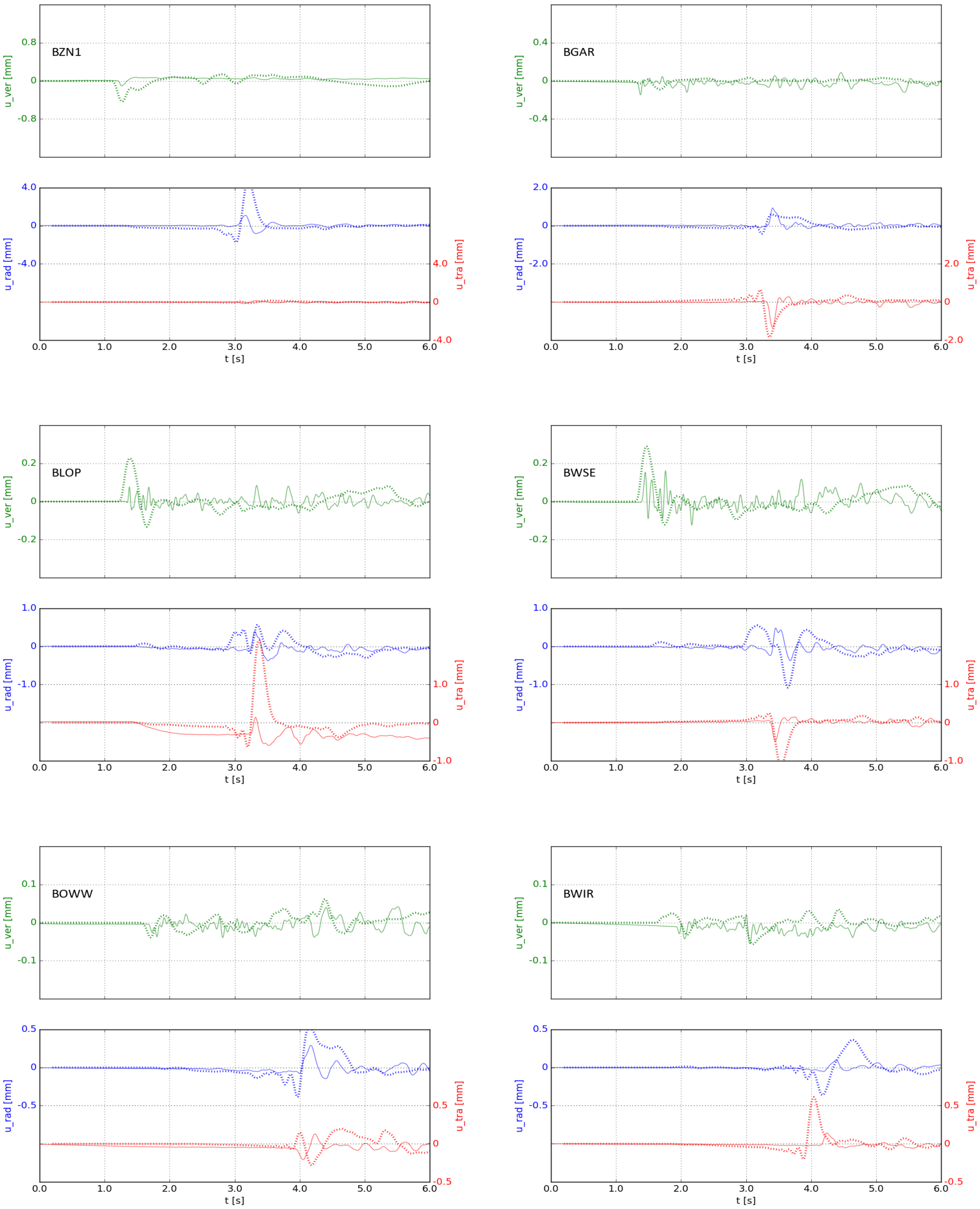

Figure 3.1 : Observed (solid) and simulated (dashed) vertical (green), radial (blue) and transverse (red) displacements following from the Zeerijp M_L 3.4 tremor, recorded by the ground accelerometers of the BZN1, BGAR, BLOP, BWSE, BOWW and BWIR stations. The simulated radial and transverse displacements have been shifted 0.2 s in time and amplified twice to include the effect of the slow down of the S wave in the shallow subsurface.

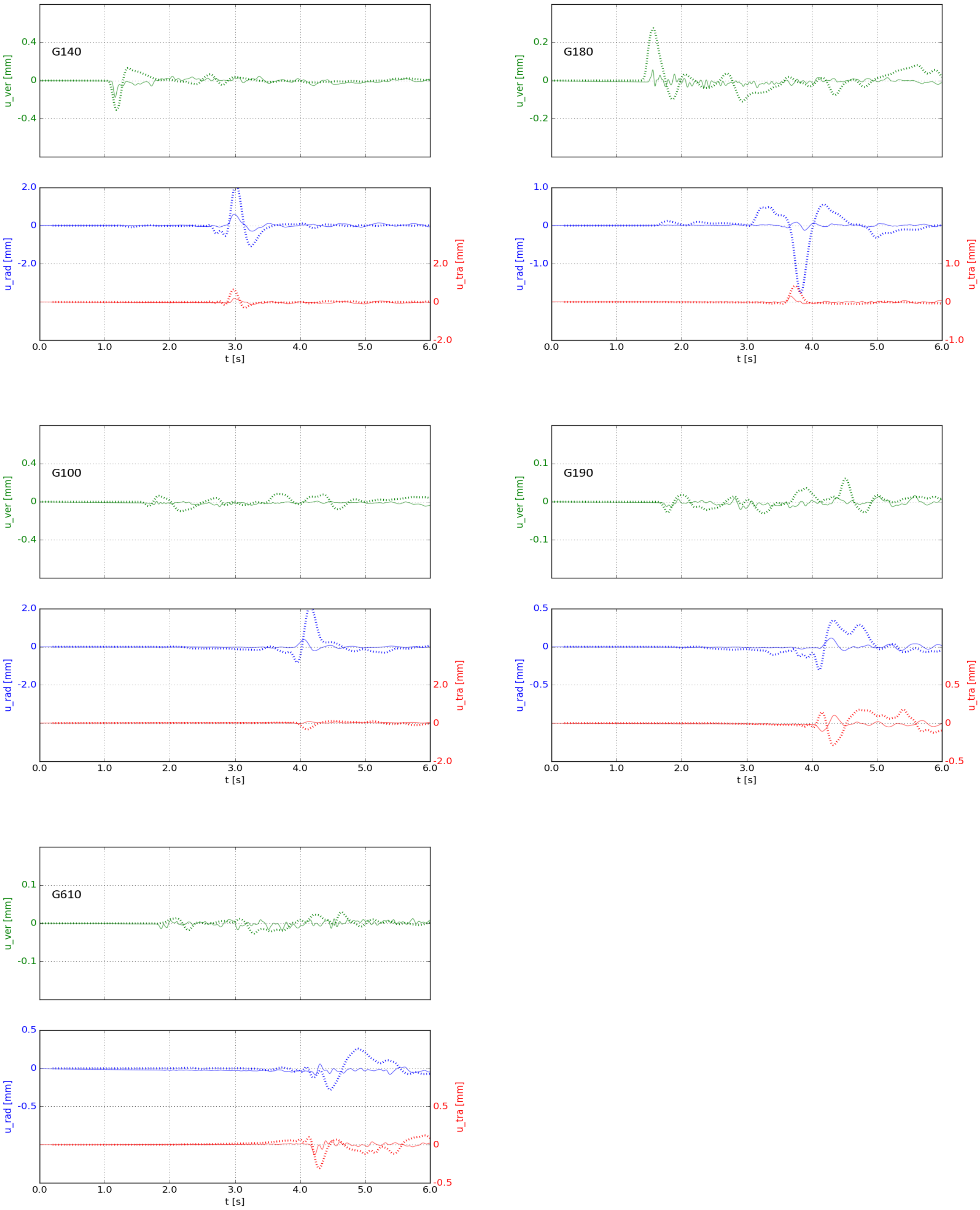

Figure 3.2 : Observed (solid) and simulated (dashed), vertical (green), radial (blue) and transverse (red) displacements following from the Zeerijp M_L 3.4 tremor, recorded by the ground accelerometers of the G14, G18, G10, G19 and G61 stations.

The simulated radial and transverse displacements have been shifted 0.2 s in time and amplified twice to include the effect of the slow down of the S wave in the shallow subsurface.

Chapter 4

Discussion

We found for several stations a reasonable correspondence between the observed and simulated displacements. Further, the results of the FEM simulations are consistent with the depth of the tremor hypocentre calculated from moment tensor inversion methods using the present velocity model of the subsurface.
However, the correspondence is less for at least two stations, e.g. G14 and G18. The use of somewhat other source parameters did not significantly reduce the present differences between the simulated and observed signals. Regarding these differences, the FEM simulations cannot be conclusive in reconstructing the rupture plane dimensions by comparing simulations and observed signals, despite the dense network of seismometers.

For most stations, the largest dimension of the slip or rupture plane of the fault seems small when compared to the distance between the hypocentre and the seismometer stations. This means that the source can be quite well approximated by a point source and, under favourable conditions, the dimensions of the slip plane can be derived from displacement spectra and/or from the apparent source time functions. These apparent source time functions can be derived using the empirical Green function method and the signals of another smaller tremor at the same hypocentre and a similar focal mechanism. Taking advantage of these methods, developed for natural earthquakes, we have determined corner frequencies of all signals of all stations and the apparent source time functions, see Appendix B. Variations of these properties over the source-receiver azimuth angle indicate that the rupture of the Zeerijp tremor propagated uni-directional along fault strike to the north west rather than along fault dip.
We have not used the apparent source time functions to constrain the extended source model in another way because the interpretation of this data needs more study. Preferably, the preliminary conclusions in this report should firstly be confirmed by experts.

Chapter 5

Acknowledgements

I thank Remco Romijn (NAM) and Clemens Visser (NAM) for providing me the field data and the velocity model, Marloes Kortekaas (EBN) and Alan Wood (SGS-I) for providing me the fault data from ant-tracking around the Zeerijp tremor epicentre, Bernard Dost (KNMI) and Ewoud van Dedem (SGS-I) for providing a plausible fault plane orientation and slip direction of the Zeerijp tremor. I thank Elmer Ruigrok (KNMI) for sharing with me apparent source time functions. I thank all, Steve Oates and Tom Piesold (SGS-I) for comments and suggestions.

Bibliography

Aki, K., and Richards, P. G., “Quantitative Seismology”, University Science Books, 2009.

Bommer, J. J., Dost, B., Edwards, B., Rodriguez-Marek, A., Kruiver, P., Meijers, P., Ntinalexis, M., and Stafford, P. J., “Development of Version 2 GMPEs for Response Spectral Accelerations and Significant Durations from Induced Earthquakes in the Groningen Field”,, Technical report, Nederlandse Aardolie Maatschappij B.V., the Netherlands, 2015.

Bommer, J. J., “Overview of Development of Current Ground-Motion Model for the Groningen Field”,, Technical Report presentation for Groningen GMPE Workshop, London, 18-20 July 2016, Independent consultants to NAM, 2016.

Burnett, W., “3D Finite Difference Wavefield Modeling for Ground Motions”,, Technical Report presentation for Groningen GMPE Workshop, London, 18-20 July 2016, ExxonMobil URC, Houston, 2016.

Dost, B., and Haak, P. J., “A Comprehensive Description of the KNMI Seismological Instrumentation”,, Technical Report Technical report TR-2452002, Koninklijk Nederlands Metereologisch Instituut, the Netherlands, 2002.

Dost, B., and Kraaijpoel, D., “The August 16, 2012 Earthquake near Huizinge (Groningen)”,, Technical Report KNMI report TR 16/1/2013, Koninklijke Nederlands Meteorologisch Instituut, the Netherlands, 2013.

Dost, B., van Eck, T., and Haak, H., “Scaling of Peak Ground Acceleration and Peak Ground Velocity Recorded in the Netherlands”, Bollettino di Geofisica Teorica ed Applicata, 45, 153–168, 2004.

Dost, B., Edwards, B., and Bommer, J. J., “The Relationship between M and M_L: A Review and Application to Induced Seismicity in the Groningen Gas Field, The Netherlands”, Seism. Res. Letters, 89, 1062–1074, 2018.

Dost, B., “Moment Tensor Solutions for Groningen Earthquakes”,, Technical Report presentation for Groningen GMPE Workshop, London, 18-20 July 2016, Koninklijke Nederlands Metereologisch Instituut, the Netherlands, 2016.

Edwards, B., Bommer, J., Stafford, P., and Rodrigues-Marek, A., “Inversion of Ground Motions for Source, Path and Site Parameters and Generation of Stochastic Records”,, Technical Report presentation for Groningen GMPE Workshop, London, 18-20 July 2016, Independent consultants to NAM, 2016.

Graves, R. W., and Pitarka, A., “Broadband Ground-Motion Simulation using a Hybrid Approach”, Bull. Seis. Soc. Am., 100, 2095–2133, 2010.

Graves, R. W., and Pitarka, A., “Refinements to the Graves and Pitarka (2010) Broadband Ground-Motion Simulation Method”, Seismological Research Letters, 86, 1–6, 2015.

Langemeijer, J., “Estimation of an Effective Velocity Model for the pre-Permian below the Northeast Netherlands”,, Technical Report Master thesis, September 2017, University Utrecht, EBN, KNMI, the Netherlands, 2017.

Lawrence, Z., Gans, C., Bailey, J., Burnett, W., Gist, G., and Reilly, J., “Groningen Seismic Observations and Independent Event QC”,, Technical Report presentation for NAM/URC Groningen Workshop, 4-6 March 2015, ExxonMobil URC, Houston, 2015.

NAM, “Geological Schematisation of the Shallow subsurface of Groningen for Site Response to Earthquakes for the Groningen gas field, Deltares report”,, Technical report, Nederlands Aardolie Maatschappij B.V., the Netherlands, 2015.

Savage, J. C., “Corner Frequency and Fault Dimensions”, Journ. of Geophysical Research, 77, 3788–3795, 1972.

Spetzler, J., and Dost, B., “Hypocentre Estimation of Induced Earthquakes in Groningen”, Geophys. J. Int., 209, 453–465, 2017.

Stafleu, J., Gunnink, J., de Lange, G., and Kruiver, P., “Shear Wave Velocity for the Upper 30 m - Combining the GeoTOP 3D Voxel Model and Seismic CPT’s”,, Technical Report presentation for workshop SoDM, 17 march 2016, TNO, Utrecht, Houston, 2016.

Stein, S., and Wysession, M., “An Introduction to Seismology, Earthquakes, and Earth Structure”, Blackwell Publishing, 2003.

Terrell, M., “Structural Overview and Max Magnitude Summary”,, Technical Report presentation for Groningen GMPE Workshop, London, 18-20 July 2016, ExxonMobil URC, Houston, 2016.

Udias, A., Madariaga, R., and Buforn, E., “Source Mechanisms of Earthquakes - Theory and Practice”, Cambridge University Press, 2014.

van Dedem, E. J., “Ground Motion Modeling for Groningen”,, Technical Report presentation for Groningen GMPE Workshop, London, 18-20 July 2016, Shell Global Solutions International, Rijswijk, 2016.

Wentinck, H. M., “Kinematic Modelling of Large Tremors in the Groningen Field using Extended Seismic Sources - First Results related to the Huizinge 2012 Tremor”,, Technical Report report for NAM, Shell Global Solutions International B.V., 2017.

Wentinck, H. M., “Dynamic Rupture Modelling - Zeerijp tremor $\mathrm{M_L}$ 3.4 in the Groningen field”,, Technical Report report for NAM, Shell Global Solutions International B.V, 2018.

———, “Kinematic Modelling of Large Tremors in the Groningen Field using Extended Seismic Sources - Second Results related to the Huizinge 2012 Tremor”,, Technical Report report for NAM, Shell Global Solutions International B.V., 2018.

Zhu, L., and Ben-Zion, Y., “Parametrization of General Seismic Potency and Moment Tensors for Source Inversion of Seismic Waveform Data”, Geophys. J. Int., 194, 839843, 2013.

Appendix A

Field data and tremor and stations coordinates

Table A.1 shows the names of the subsurface formations used in the seismic velocity model 2015 and the mean depths of the lower horizons and the thickness of these formations around Zeerijp. Table A.2 shows the rock types in these formations. Table A.3 shows the parameters used for the velocity model. Figure A.1 shows the P and S wave velocity profiles used.

Table A.4 shows the Dutch Rijksdriehoeksstelsel (RD) coordinates of the epicentre of the Zeerijp M_L 3.4 tremor, the nearby seismometer stations and the distance between them and the tremor epicentre.
It also shows corrections for the orientations of the ground accelerometers and the orientations of the geophones in the shallow boreholes at 50 - 200 m depth in the horizontal plane. They have been determined in a collaborative effort by KNMI and SGS-I using calibration shots and very large earthquakes from other continents. Using more data, the corrections are regularly updated and available in the form of Excel spreadsheets. The KNMI data shown originates from the previous version of end 2017. For the stations used, updated orientations of May 2018 deviate less than a few degrees from the version of late 2017.
In Table A.4 , the angles of rotation are in the following order: 0,1,2,3,4 where 0 stands for the ground accelerometer and 1,2,3,4 stands for the geophones at 50, 100, 150 and 200 m depth, respectively. For the G stations, these relate to the orientations of HH1 sensor of the ground accelerometer (0) and the orientation of the HH2 sensor of geophones 1,2,3,4 with respect to the north direction. For the B stations, the second column shows the HN sensor orientation of the ground accelerometer.

Table A.1 : Mean depths of the lower horizon (or the base) of the formations around the Zeerijp tremor epicentre which are used in the seismic velocity model of NAM, update 2015 in a 3×3 km area around the Zeerijp tremor with the following RD centre coordinates: X = 245 km and Y = 598 km. The Rijnland, Altena and Triassic formations are combined in the model to form a single formation.

Formation name used	mean depth lower horizon m	mean thickness m
Upper North Sea	-323	323
Lower North Sea	-810	477
Chalk	-1700	890
Rijnland	-1771	71
Altena	-1772	1
Triassic	-1965	193
Upper Zechstein	-2250	285
floater	-2293	43
Lower Zechstein	-2802	509
anhydrite	-2852	50
Rotliegend reservoir	-3120	268
Carboniferous underburden	-5903	2783

Table A.2 : Rock type of the formations in the seismic velocity model 2015 of NAM.

formation name	rock type
Upper North Sea	Quarternary shallow marine to terrestial clay and fine to course sands
Lower North Sea	Tertiary shallow marine clays, sands and sandstones
Chalk	Cretaceous shallow to deep-marine limestone
Rijnland	Cretaceous shallow marine marlstone, claystone and interbedded sandstones
Altena	Jurassic marine claystone
Triassic	Triassic lower Bundsandstein formation: lacustrine claystone, siltstone and very fine sandstone
upper Zechstein	Zechstein evaporite, rock salt
floater	Zechstein floater, anhydrite
lower Zechstein	Zechstein evaporite, rock salt
anhydrite	Anhydrite and dolomite
Rotliegend reservoir	Ten Boer claystone - lacustrine shale with thin sandstone Slochteren sandstone reservoir - mixed fluvial-aeolian sandstone
Late Carboniferous underburden	lacustrine and floodplain siltstones, organic shales and lower delta plain fine sandstones

Table A.3 : Input parameters for the velocity model 2015 of NAM for the various subsurface formations and used in the FEM simulations.

formation name	$V_{p,0}$ m/s	k_p 1/s	$V_{s,0}$ m/s	k_s 1/s
Upper North Sea	1733	0.500	458	0.430
Lower North Sea	1922	0.500	614	0.430
Chalk	680	2.300	-5	1.390
Rijnland	2125	0.500	701	0.420
Altena	2222	0.355	1364	0.190
Triassic	2383	0.680	1450	0.380
upper Zechstein	4300	0	2436	0
floater	5729	0	3152	0
lower Zechstein	4475	0	2524	0
anhydrite	6000	0	3288	0
Rotliegend reservoir	3800	0	2232	0
Carboniferous underburden	2572	0.541	837	0.500

Table A.4 : The Dutch Rijksdriehoeksstelsel (RD) coordinates of the epicentre of the Zeerijp tremor and the KNMI stations used. For the G stations, the second column gives the orientations of the accelerometers and the geophones, see text. The last column gives the distance between the tremor epicentre and the stations.

name	orientation degrees	X m	Y m	dist. km
tremor				
Zeerijp 2018/01/028	KNMI	245714	597574	
	SGS-I	245600	597600	
shallow borehole station				
G14	356,143,275,358,333	247117	597798	1.4
G18	0,267,281,137,317	243906	594620	3.5
G10	0,281,22,39,246	249310	600056	4.4
G19	0,170,162,330,94	250238	595543	5.0
G61	0,335,131,206,301	241112	600280	5.3
G23	0,174,159,269,178	247002	592330	5.4
G13	0,174,159,269,178	240332	596592	5.5
G62	0,222,195,142,4	251786	601052	7.0
G04	10,182,152,281,83	240607	603922	8.1
ground accelerometer station				
BZN1	-9	247389	598590	2.0
BGAR	359	243289	598757	2.7
BLOP	352	245560	595020	2.6
BWSE	359	243091	596144	3.0
BOWW	352	249933	595841	4.6
BWIR	341	248213	593808	4.5

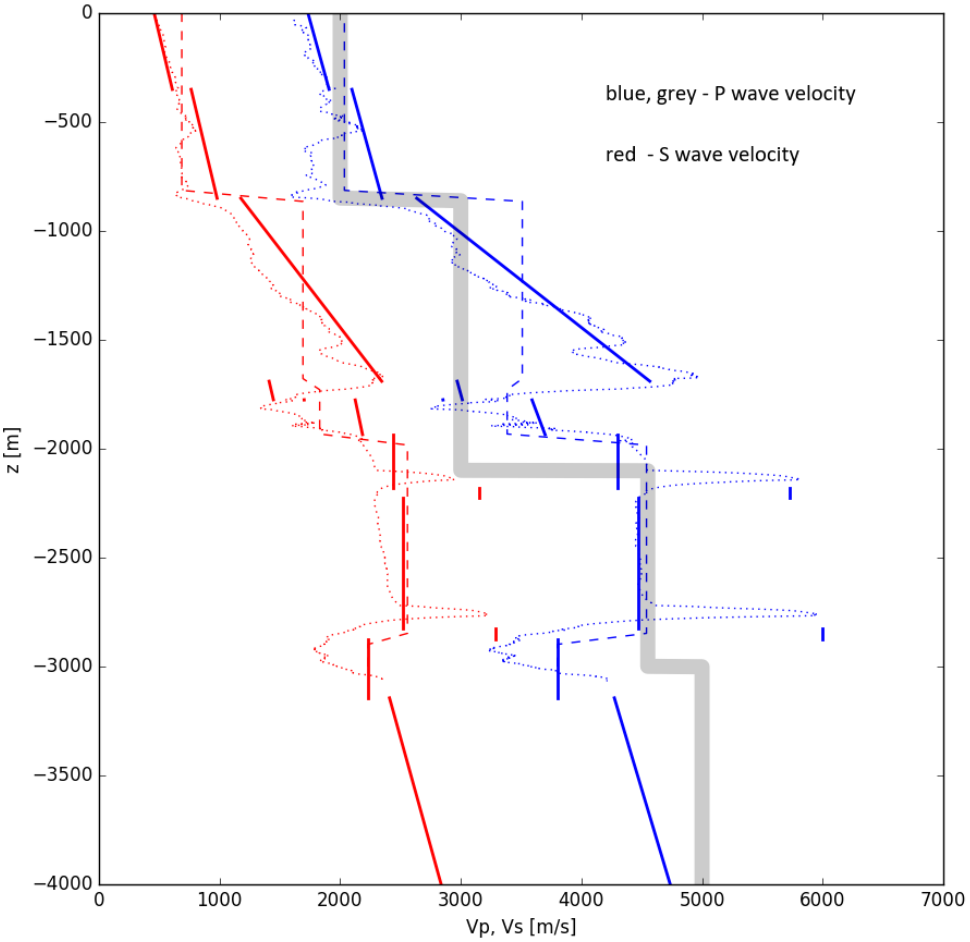

Figure A.1 : P and S wave velocity profiles. The solid line shows the wave velocities used in the FEM simulations. The dashed lines are the wave velocities used for calculating wave travel times with ray tracing, see §B.4. The thin dotted lines are the wave velocities measured in the Stedum observation well, within 5 km east from the tremor epicentre. For reference, the thick grey solid line shows the P wave velocity according to the 1D tremor hypocentre model from KNMI, which is an average model that is representative for the northern part of the Netherlands, see Spetzler and Dost (2017), Figure 7. In the Triassic, Altena, Rijnland and Chalk formations, the P wave velocity is substantially lower than the one we use for ray tracing.

Appendix B

Additional recordings

Appendix B.1 Recorded displacements and spectra

Figures B.1 - B.15 show the radial, transverse and vertical displacements recorded by the ground accelerometers and geophones, spectra of these displacements and the apparent source time functions as discussed in §B.3 below[1].
The spectra or absolute values of the Fourier transforms of the displacement components use signals over a period of about 13 s starting 1 - 2 seconds before the arrival of the P wave. The spectra show low, intermediate and high frequency asymptotes, see §B.2. They decay as f^{-n}, the first roughly with power $n \sim 2$ and the second one roughly with power $n \sim 4$, see §B.2.

For the ground accelerometers of the G and B stations, the displacements follow from the following signal processing steps:

- The signals are divided by a factor 2.14 10^5 to convert them from counts into accelerations in [m/s^2].
- The signals are transformed to radial, transverse and vertical signals using the orientations and locations of the ground accelerometer and location of the tremor epicentre.
- After subtracting an unneeded constant bias, the accelerations are integrated once in the time domain to obtain the displacement velocity and once in the frequency domain to calculate the corresponding displacements.
- The displacements are filtered by a 2^{nd} order high pass filter with a cut-off frequency at 0.2 Hz to remove low-frequency disturbances in the signals.

For the geophones of the G stations, the displacements follow from the following signal processing steps:

---

[1] The displacements originate from signals contained in so-called Mini-SEED files. These are available from the Seismic and Acoustic Data Portal of the KNMI website.

- The signals are divided by a factor 2.50 10^8 to convert them from counts into velocities in [m/s].
- The signals are transformed to radial, transverse and vertical signals using the orientations and location of each geophone in the borehole and the location of the tremor epicentre.
- After subtracting unneeded constant bias, the velocities are integrated in the frequency domain to calculate the corresponding displacements.
- The frequency dependent response of the geophone below 4.5 Hz is compensated by an inverted response in the frequency domain, see §B.5.
- The displacements are filtered by a 4^{th} order high pass filter with a cut-off frequency at 0.5 Hz to remove low-frequency noise in the signals.

After taking the Fourier transforms in the complex plane, the integration from displacement velocity to displacement and filtering takes place in the frequency domain. The response and filter functions are shown in §B.5, Figure B.22 .
The choice of 0.2 Hz for the cut-off frequency of the high pass filter in the last processing step is a compromise to process the data of all stations in the same way, to use as much as possible data to determine the low frequency asymptote, and herewith the low corner frequency of the seismic source, and to minimise the contribution of low frequency electronic disturbances to the displacements.
The absolute value of the time lines in these figures is not related to the generation of the tremor and has no special meaning.

The figures show that the spectra quite differ for various stations and displacement components. Some have a more or less pronounced peak around 12 Hz.

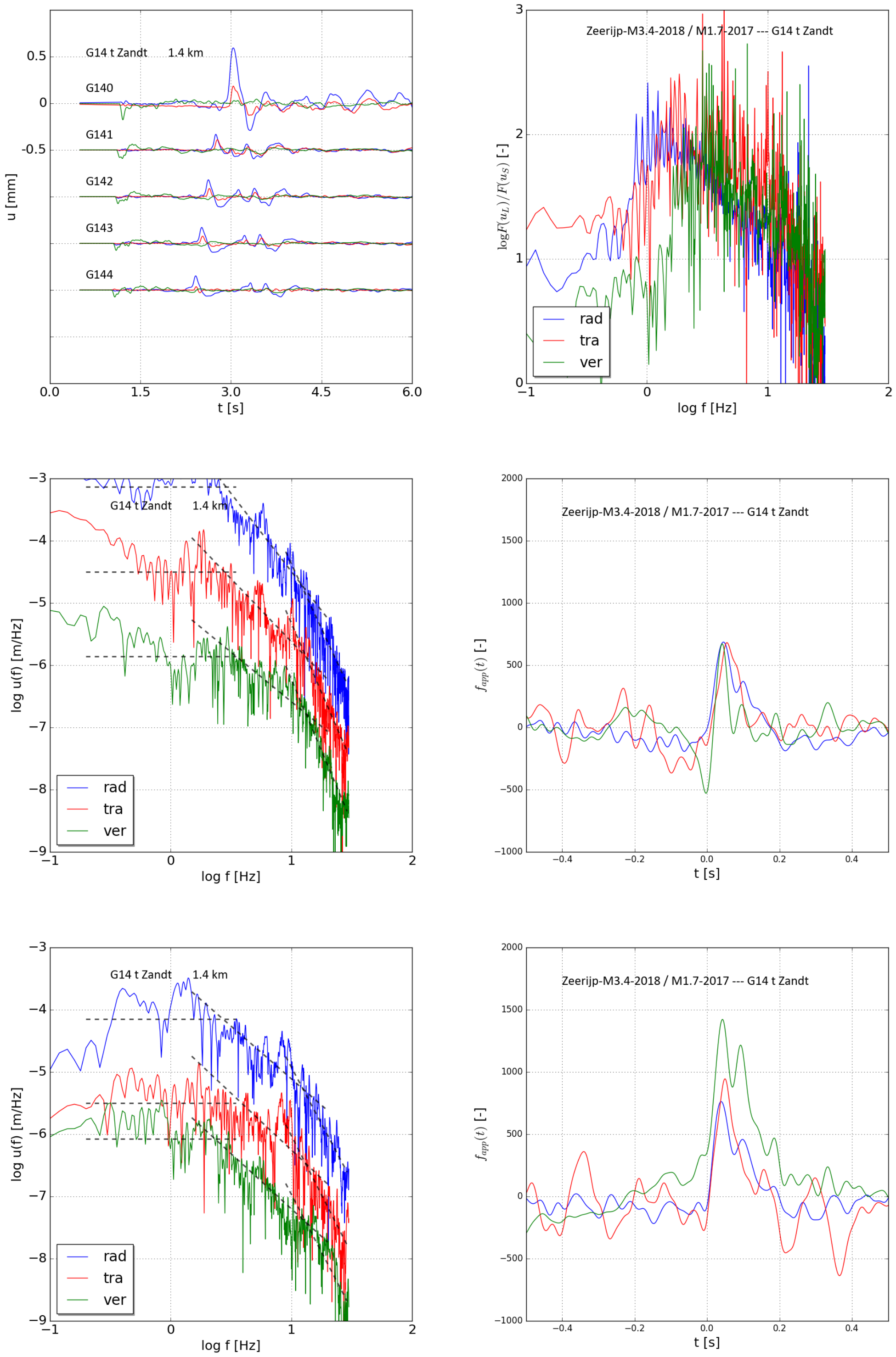

Figure B.1 : Station G14: radial (blue), transverse (red) and vertical (green) displacements (top-left) and related spectra of the accelerometers (centre-left) and geophones (bottom-left). For a better display, the spectrum of the vertical component is shifted a factor 10 down and the one of the radial component is shifted a factor 10 up. The grey dashed lines show the low, intermediate and high frequency asymptotes, respectively. The low and high corner frequencies follow from the two intersections of the asymptotes.
Quotient of spectra Q (top-right) and apparent source time functions $\dot{f}_{app}(t)$ from the accelerometer (centre-right). An average of the apparent source time functions $\dot{f}_{app}$ from the geophones at 50, 100, 150 and 200 m depth (bottom-right).

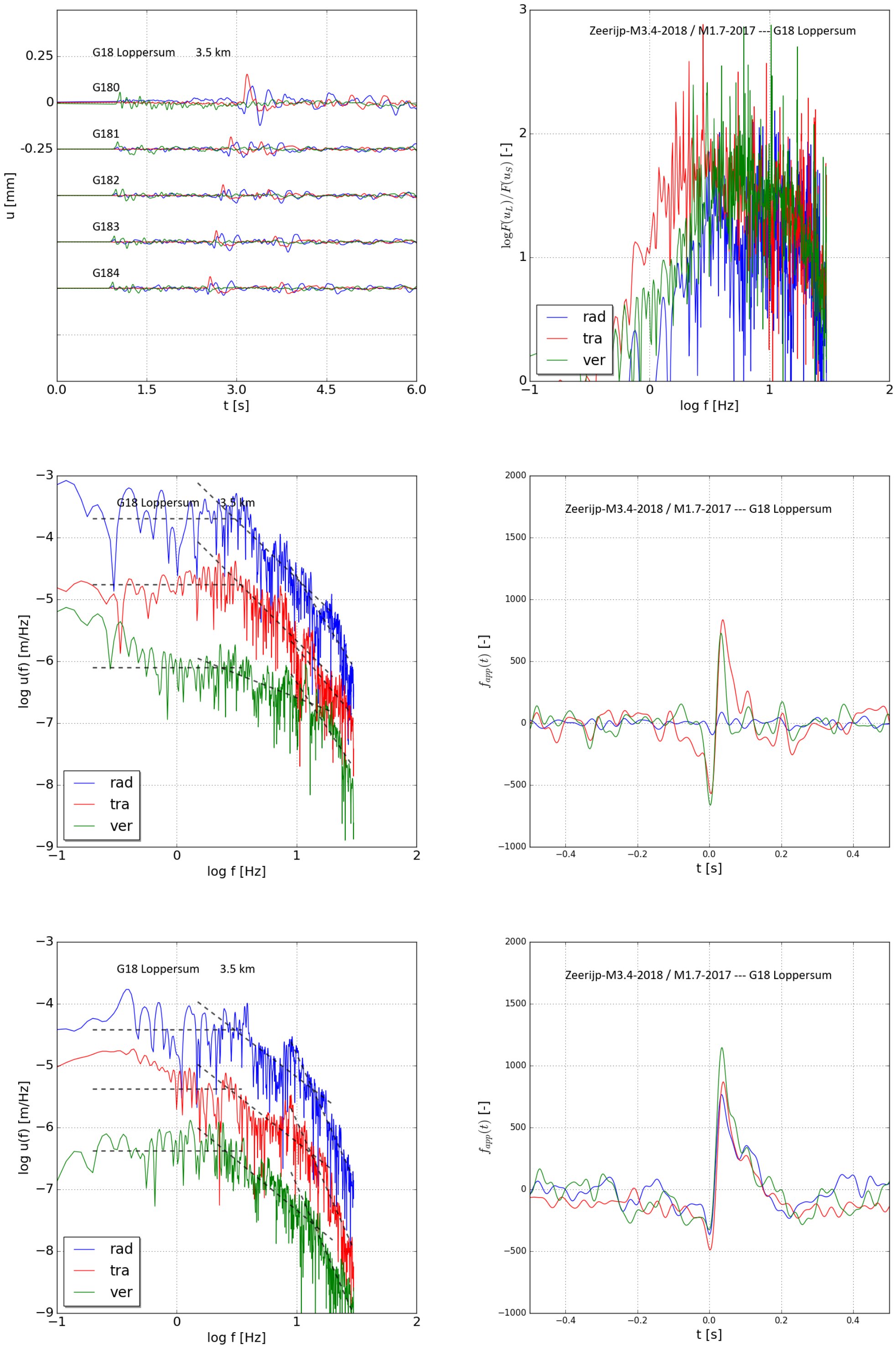

Figure B.2 : Station G18: radial (blue), transverse (red) and vertical (green) displacements (top-left) and related spectra of the accelerometers (centre-left) and geophones (bottom-left). For a better display, the spectrum of the vertical component is shifted a factor 10 down and the one of the radial component is shifted a factor 10 up. The grey dashed lines show the low, intermediate and high frequency asymptotes, respectively. The low and high corner frequencies follow from the two intersections of the asymptotes.
Quotient of spectra Q (top-right) and apparent source time functions $\dot{f}_{app}(t)$ from the accelerometer (centre-right). An average of the apparent source time functions $\dot{f}_{app}$ from the geophones at 50, 100, 150 and 200 m depth (bottom-right).

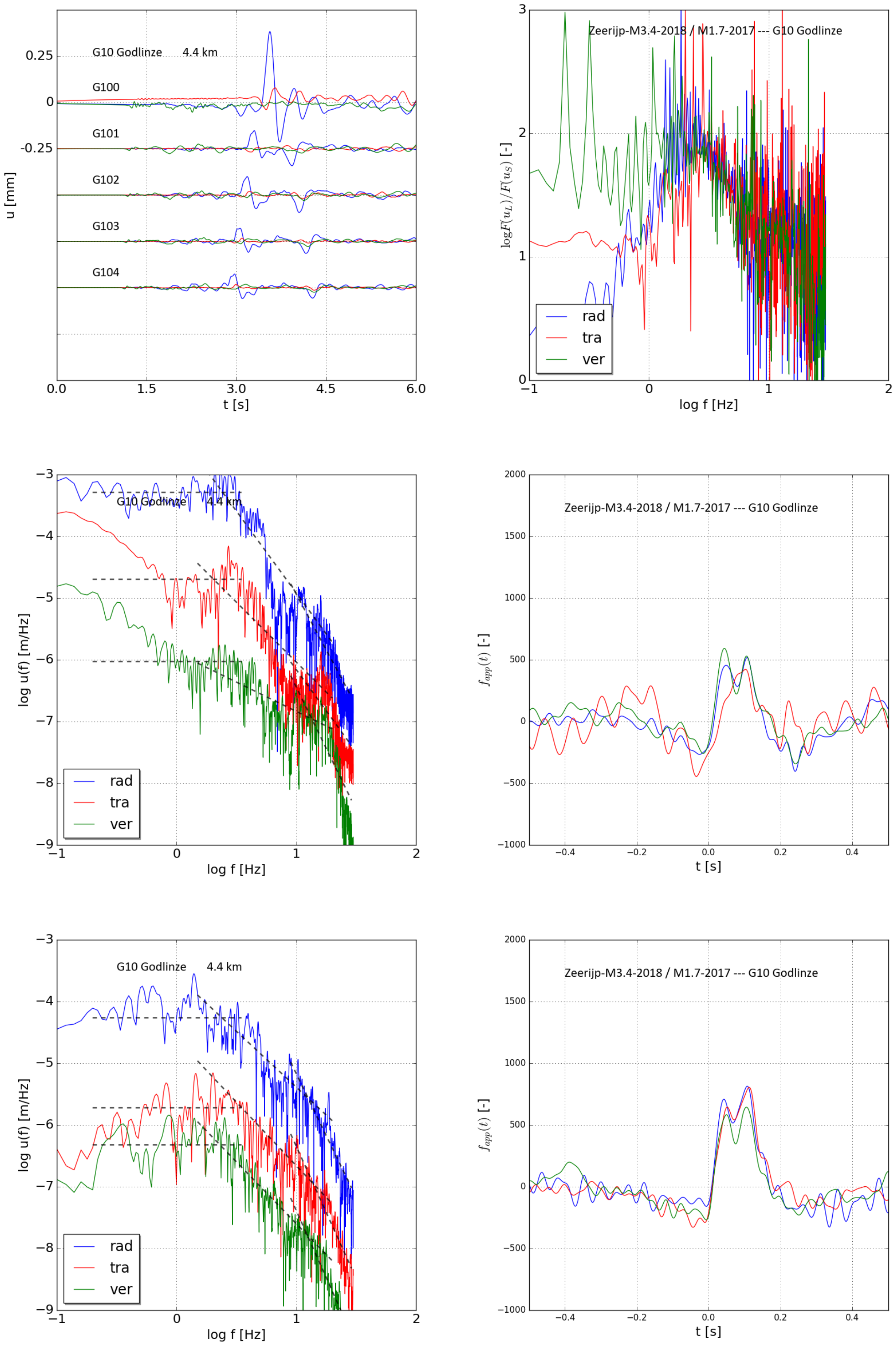

Figure B.3 : Station G10: radial (blue), transverse (red) and vertical (green) displacements (top-left) and related spectra of the accelerometers (centre-left) and geophones (bottom-left). For a better display, the spectrum of the vertical component is shifted a factor 10 down and the one of the radial component is shifted a factor 10 up. The grey dashed lines show the low, intermediate and high frequency asymptotes, respectively. The low and high corner frequencies follow from the two intersections of the asymptotes.
Quotient of spectra Q (top-right) and apparent source time functions $\dot{f}_{app}(t)$ from the accelerometer (centre-right). An average of the apparent source time functions $\dot{f}_{app}$ from the geophones at 50, 100, 150 and 200 m depth (bottom-right).

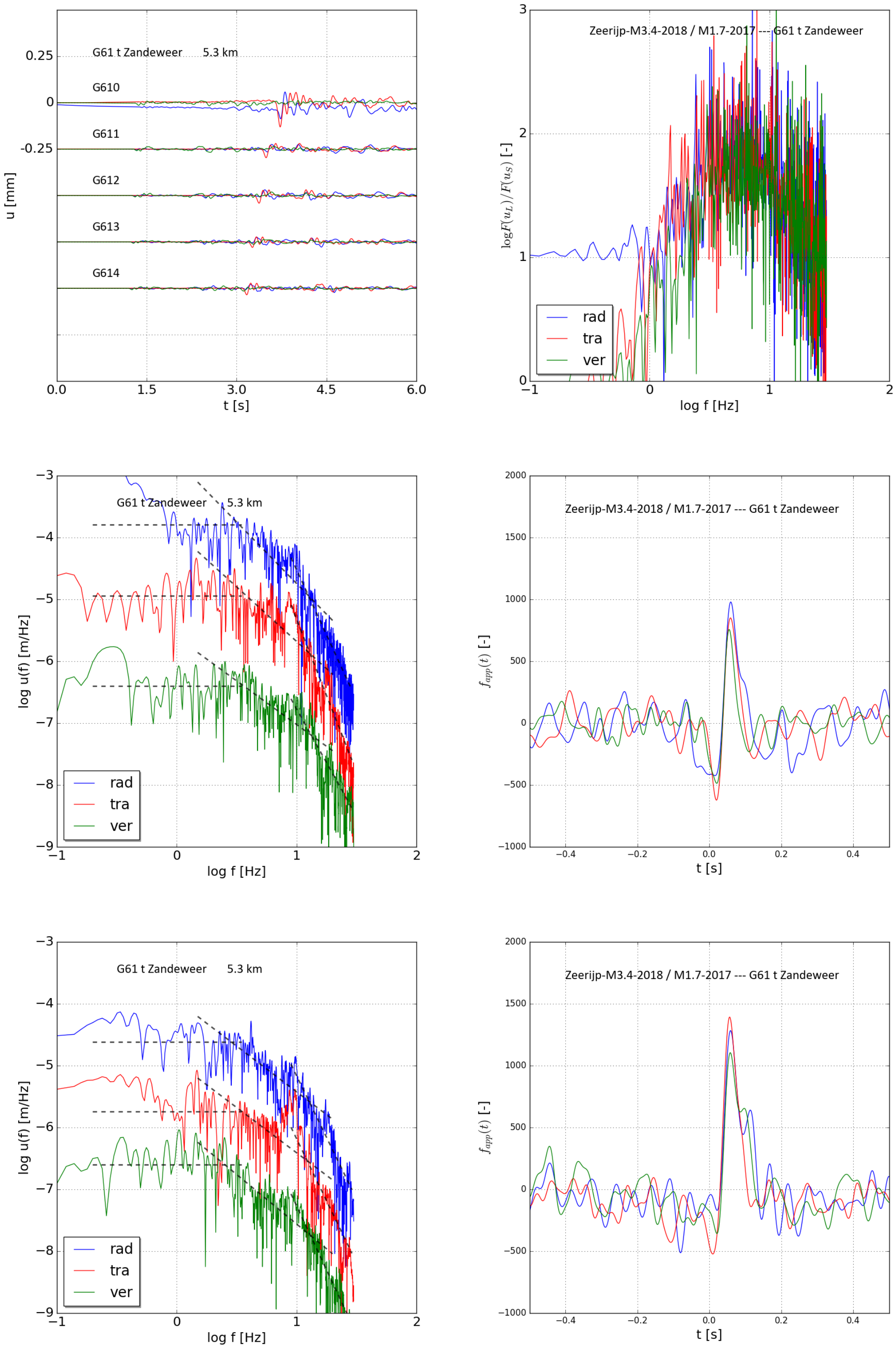

Figure B.4 : Station G61: radial (blue), transverse (red) and vertical (green) displacements (top-left) and related spectra of the accelerometers (centre-left) and geophones (bottom-left). For a better display, the spectrum of the vertical component is shifted a factor 10 down and the one of the radial component is shifted a factor 10 up. The grey dashed lines show the low, intermediate and high frequency asymptotes, respectively. The low and high corner frequencies follow from the two intersections of the asymptotes.
Quotient of spectra Q (top-right) and apparent source time functions $\dot{f}_{app}(t)$ from the accelerometer (centre-right). An average of the apparent source time functions $\dot{f}_{app}$ from the geophones at 50, 100, 150 and 200 m depth (bottom-right).

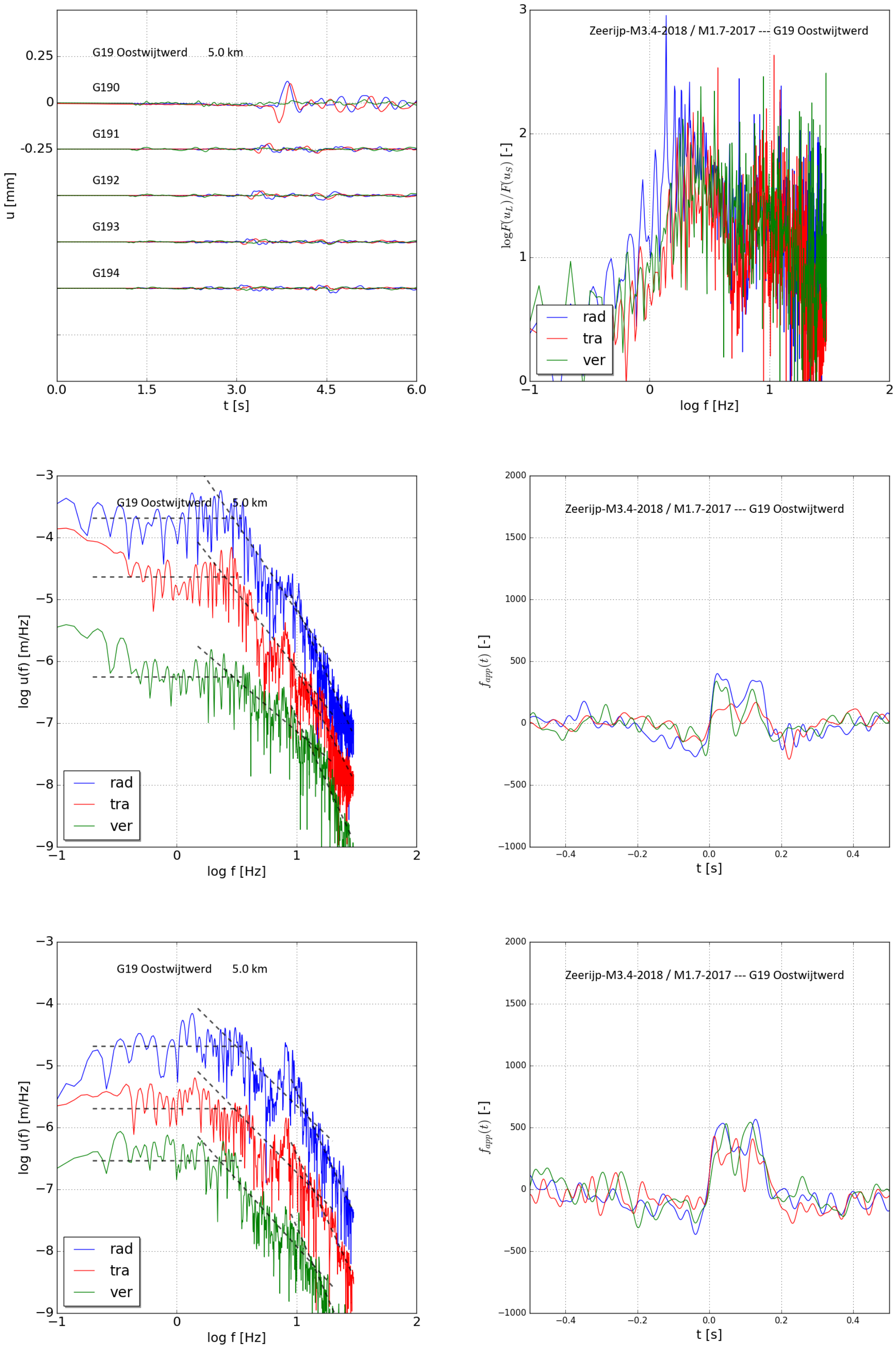

Figure B.5 : Station G19: radial (blue), transverse (red) and vertical (green) displacements (top-left) and related spectra of the accelerometers (centre-left) and geophones (bottom-left). For a better display, the spectrum of the vertical component is shifted a factor 10 down and the one of the radial component is shifted a factor 10 up. The grey dashed lines show the low, intermediate and high frequency asymptotes, respectively. The low and high corner frequencies follow from the two intersections of the asymptotes. Quotient of spectra Q (top-right) and apparent source time functions $\dot{f}_{app}(t)$ from the accelerometer (centre-right). An average of the apparent source time functions $\dot{f}_{app}$ from the geophones at 50, 100, 150 and 200 m depth (bottom-right).

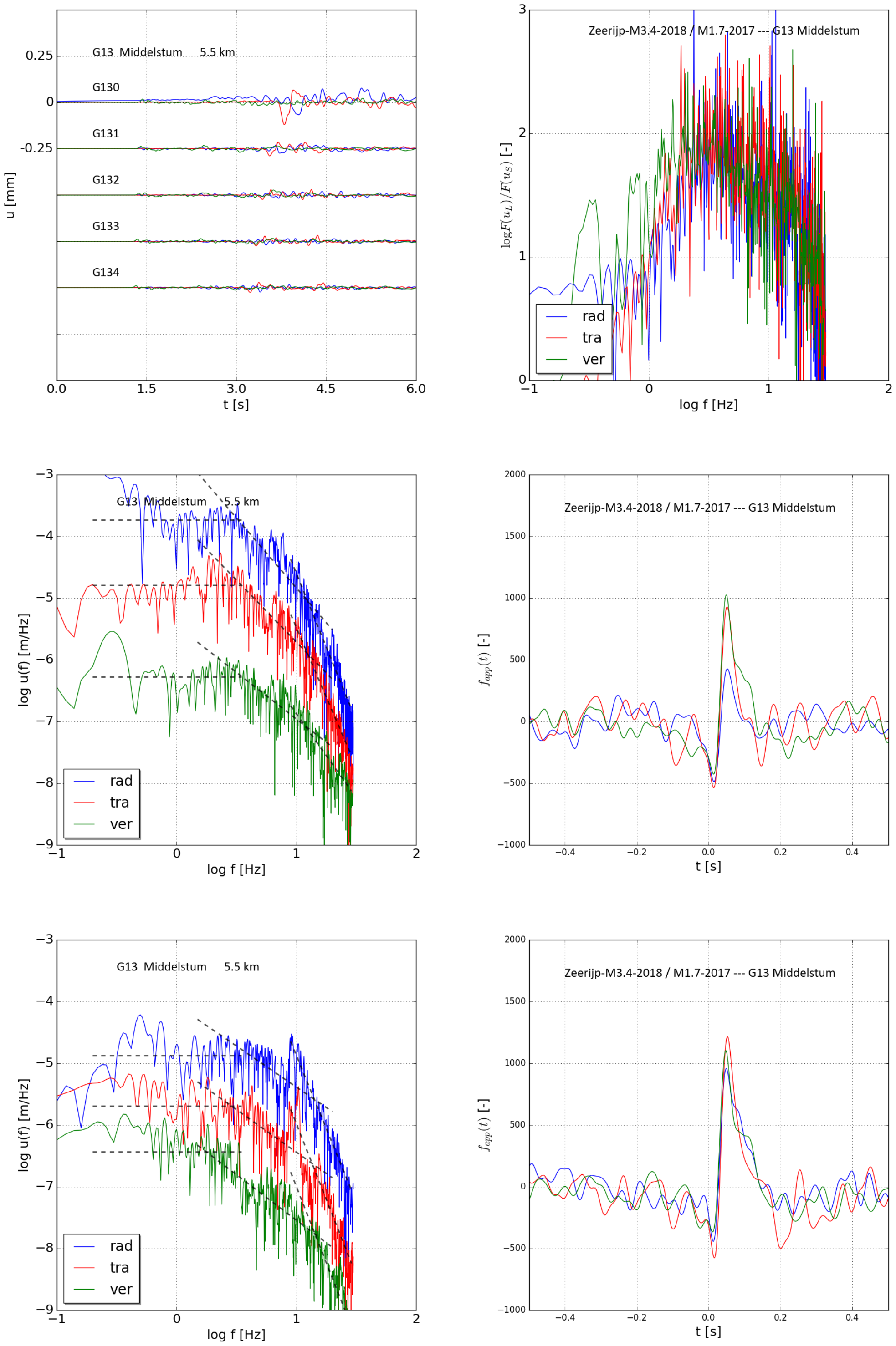

Figure B.6 : Station G13: radial (blue), transverse (red) and vertical (green) displacements (top-left) and related spectra of the accelerometers (centre-left) and geophones (bottom-left). For a better display, the spectrum of the vertical component is shifted a factor 10 down and the one of the radial component is shifted a factor 10 up. The grey dashed lines show the low, intermediate and high frequency asymptotes, respectively. The low and high corner frequencies follow from the two intersections of the asymptotes.
Quotient of spectra Q (top-right) and apparent source time functions $\dot{f}_{app}(t)$ from the accelerometer (centre-right). An average of the apparent source time functions $\dot{f}_{app}$ from the geophones at 50, 100, 150 and 200 m depth (bottom-right).

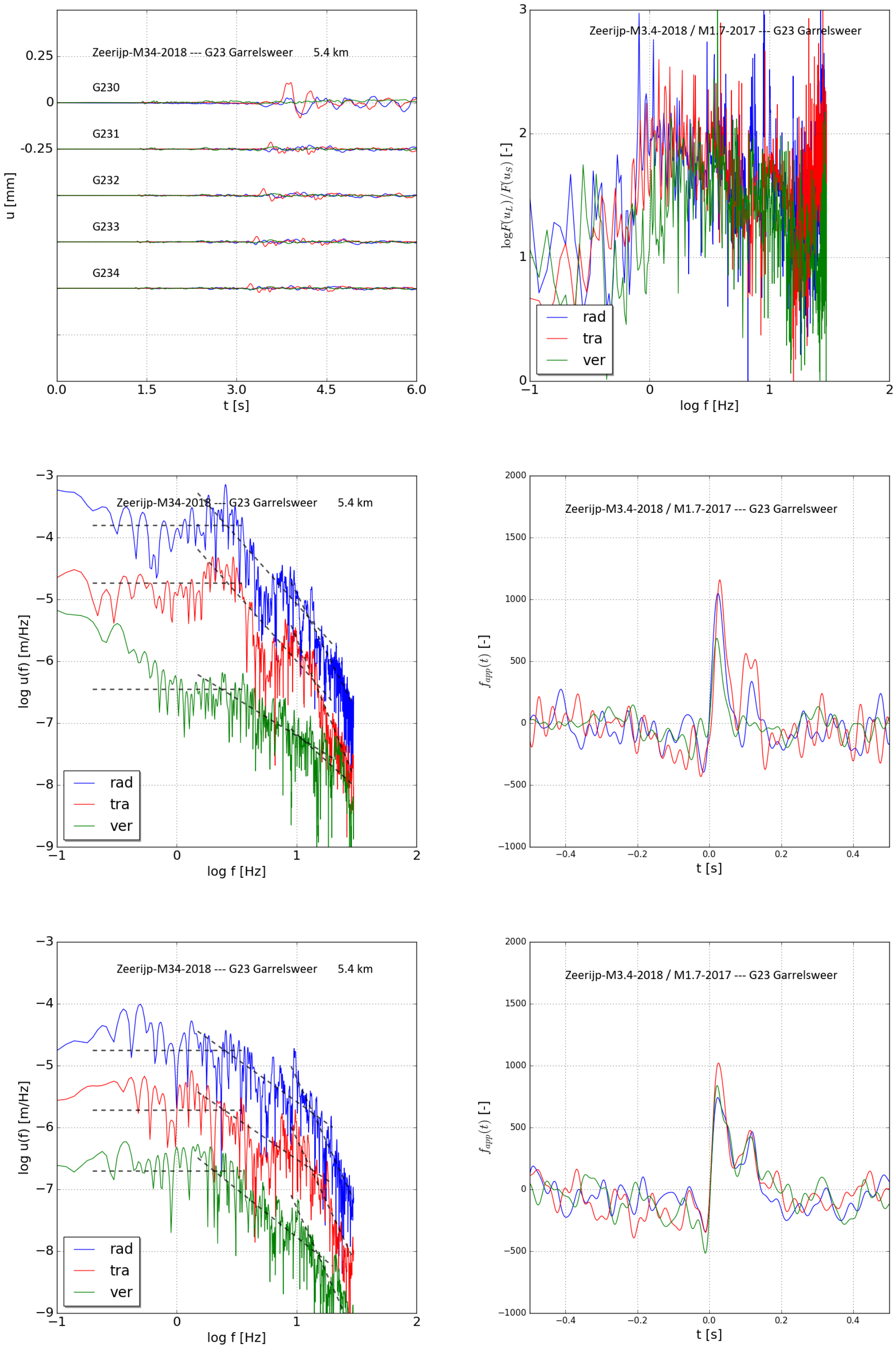

Figure B.7 : Station G23: radial (blue), transverse (red) and vertical (green) displacements (top-left) and related spectra of the accelerometers (centre-left) and geophones (bottom-left). For a better display, the spectrum of the vertical component is shifted a factor 10 down and the one of the radial component is shifted a factor 10 up. The grey dashed lines show the low, intermediate and high frequency asymptotes, respectively. The low and high corner frequencies follow from the two intersections of the asymptotes.
Quotient of spectra Q (top-right) and apparent source time functions $\dot{f}_{app}(t)$ from the accelerometer (centre-right). An average of the apparent source time functions $\dot{f}_{app}$ from the geophones at 50, 100, 150 and 200 m depth (bottom-right).

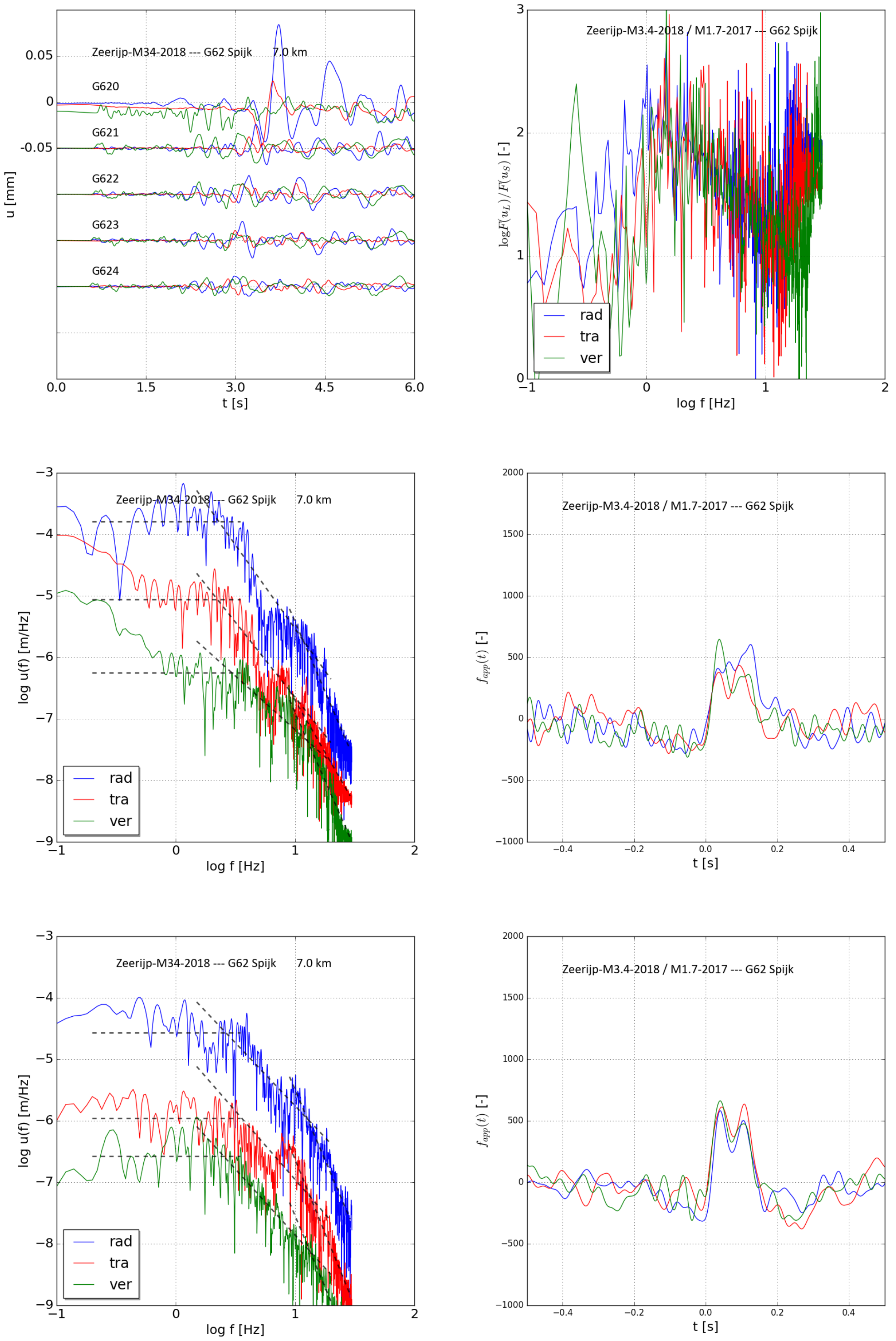

Figure B.8 : Station G62: radial (blue), transverse (red) and vertical (green) displacements (top-left) and related spectra of the accelerometers (centre-left) and geophones (bottom-left). For a better display, the spectrum of the vertical component is shifted a factor 10 down and the one of the radial component is shifted a factor 10 up. The grey dashed lines show the low, intermediate and high frequency asymptotes, respectively. The low and high corner frequencies follow from the two intersections of the asymptotes. Quotient of spectra Q (top-right) and apparent source time functions $\dot{f}_{app}(t)$ from the accelerometer (centre-right). An average of the apparent source time functions $\dot{f}_{app}$ from the geophones at 50, 100, 150 and 200 m depth (bottom-right).

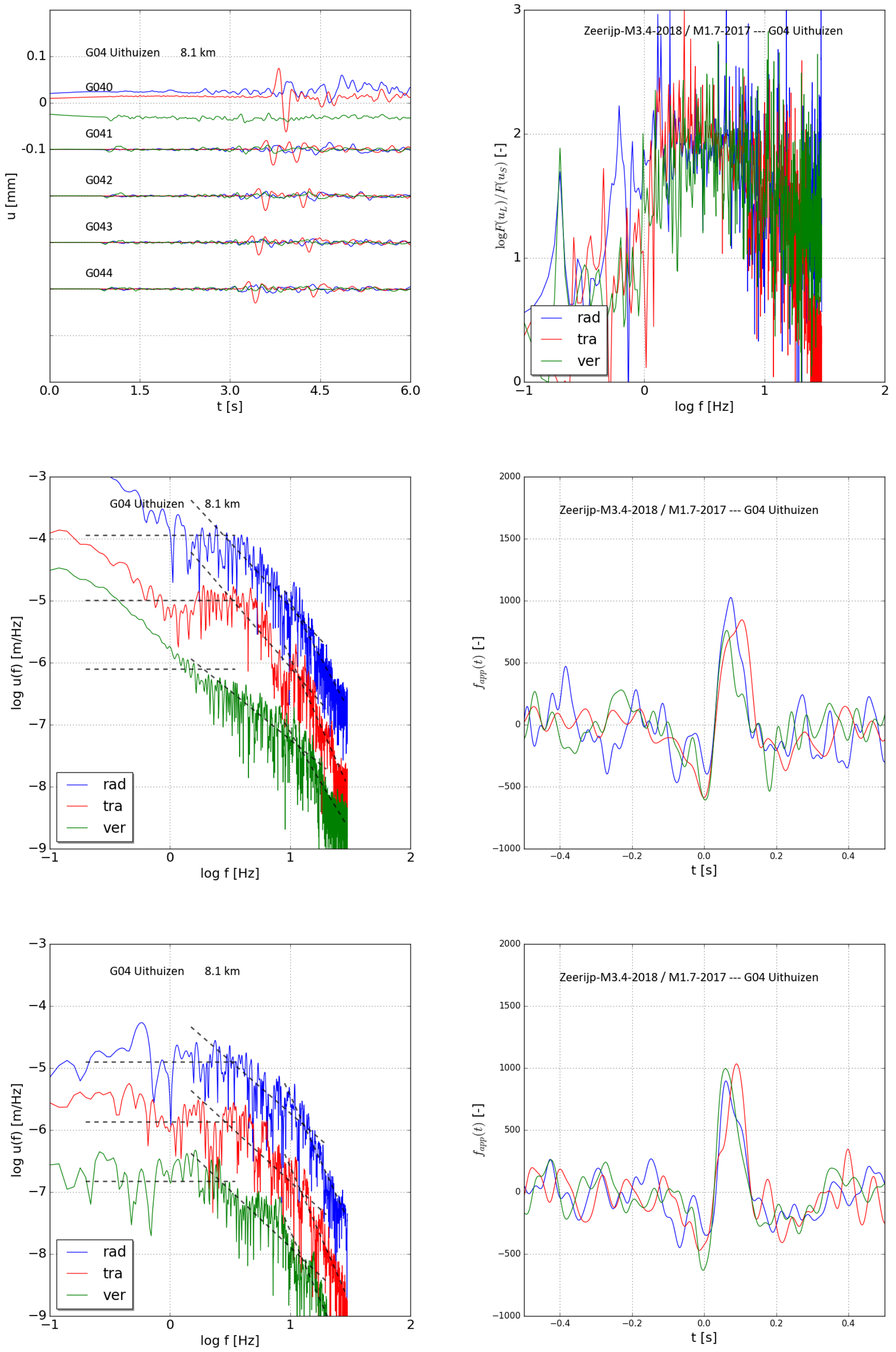

Figure B.9 : Station G04: radial (blue), transverse (red) and vertical (green) displacements (top-left) and related spectra of the accelerometers (centre-left) and geophones (bottom-left). For a better display, the spectrum of the vertical component is shifted a factor 10 down and the one of the radial component is shifted a factor 10 up. The grey dashed lines show the low, intermediate and high frequency asymptotes, respectively. The low and high corner frequencies follow from the two intersections of the asymptotes. Quotient of spectra Q (top-right) and apparent source time functions $\dot{f}_{app}(t)$ from the accelerometer (centre-right). An average of the apparent source time functions $\dot{f}_{app}$ from the geophones at 50, 100, 150 and 200 m depth (bottom-right).

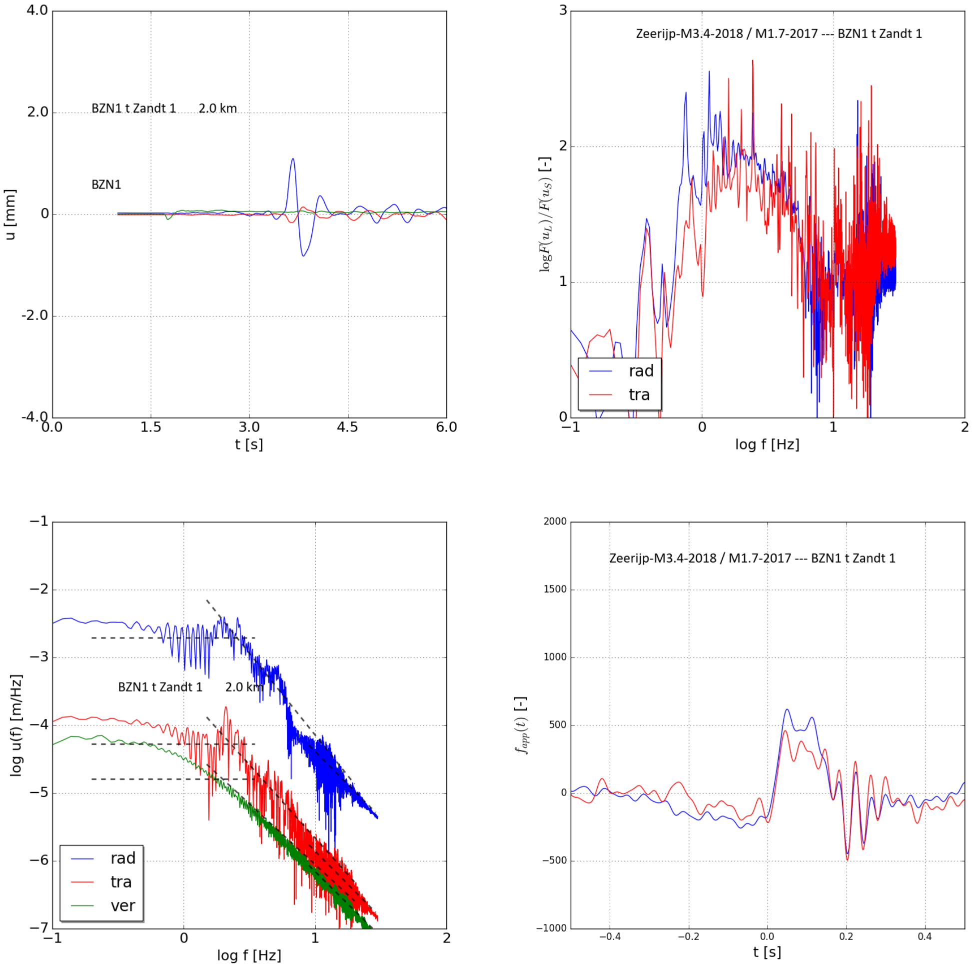

Figure B.10 : Station BZN1: radial (blue), transverse (red) and vertical (green) displacements (top-left) and related spectra of the accelerometers (bottom-left). For a better display, the spectrum of the vertical component is shifted a factor 10 down and the one of the radial component is shifted a factor 10 up. The grey dashed lines show the low, intermediate and high frequency asymptotes, respectively. The low and high corner frequencies follow from the two intersections of the asymptotes.
Quotient of spectra Q (top-right) and apparent source time functions $\dot{f}_{app}(t)$ from the accelerometer (bottom-right).

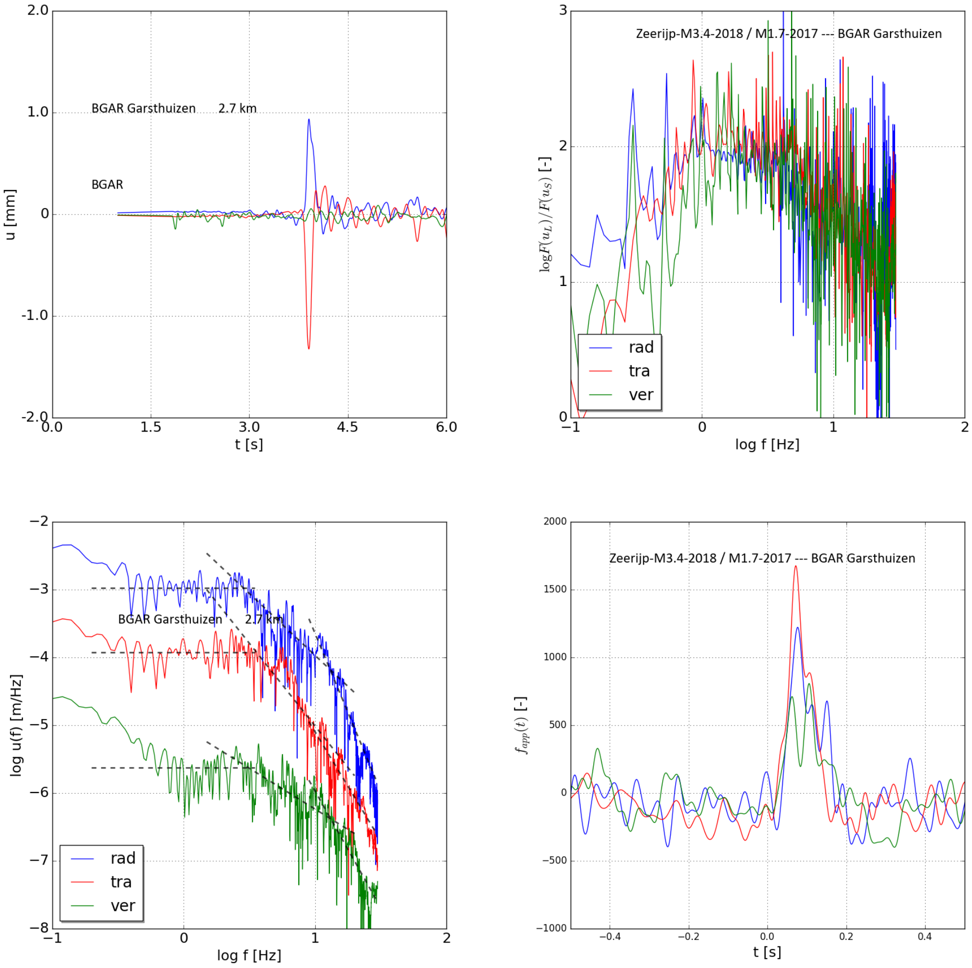

Figure B.11 : Station BGAR: radial (blue), transverse (red) and vertical (green) displacements (top-left) and related spectra of the accelerometers (bottom-left). For a better display, the spectrum of the vertical component is shifted a factor 10 down and the one of the radial component is shifted a factor 10 up. The grey dashed lines show the low, intermediate and high frequency asymptotes, respectively. The low and high corner frequencies follow from the two intersections of the asymptotes.
Quotient of spectra Q (top-right) and apparent source time functions $\dot{f}_{app}(t)$ from the accelerometer (bottom-right).

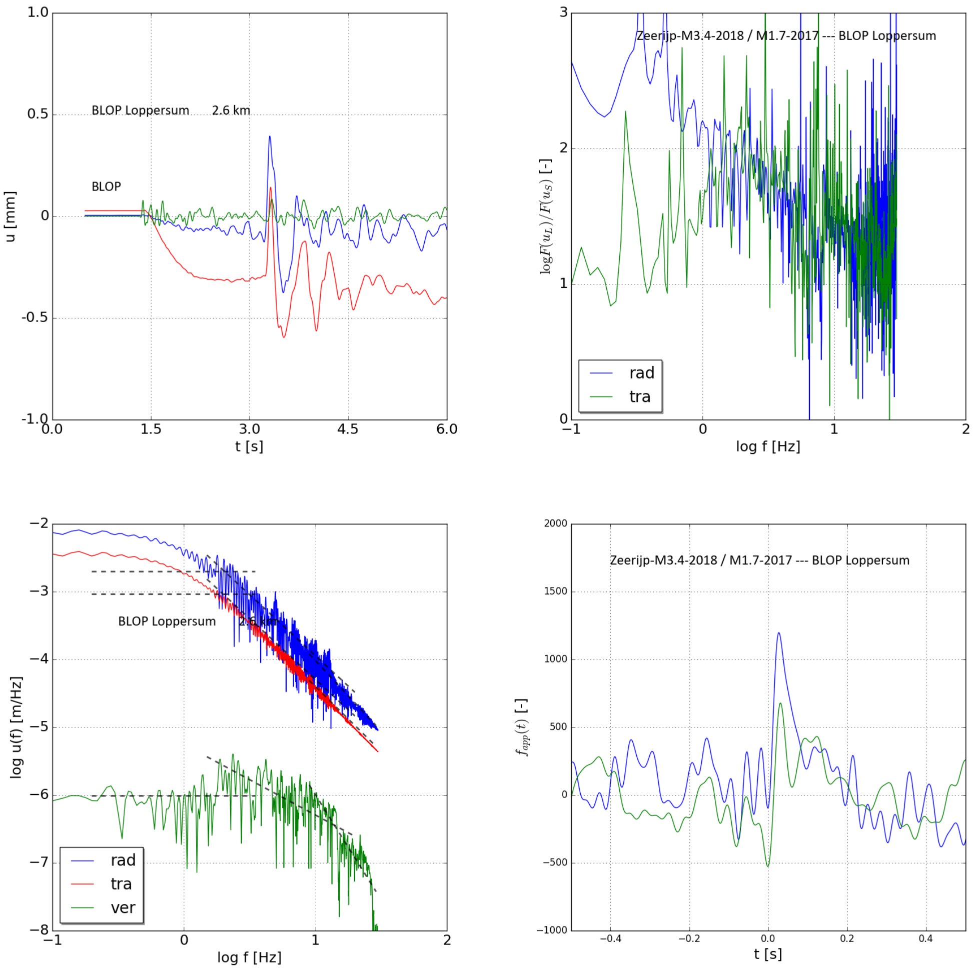

Figure B.12 : Station BLOP: radial (blue), transverse (red) and vertical (green) displacements (top-left) and related spectra of the accelerometers (bottom-left). For a better display, the spectrum of the vertical component is shifted a factor 10 down and the one of the radial component is shifted a factor 10 up. The grey dashed lines show the low, intermediate and high frequency asymptotes, respectively. The low and high corner frequencies follow from the two intersections of the asymptotes.
Quotient of spectra Q (top-right) and apparent source time functions $\dot{f}_{app}(t)$ from the accelerometer (bottom-right).

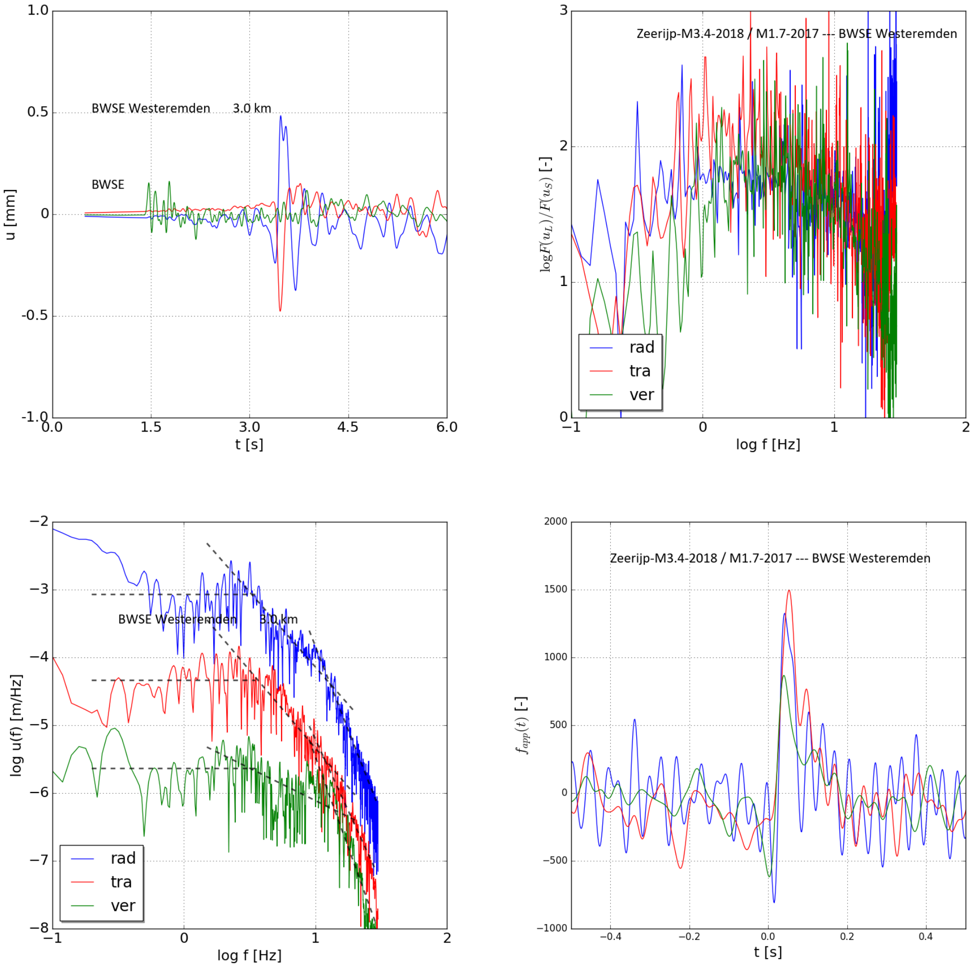

Figure B.13 : Station BWSE: radial (blue), transverse (red) and vertical (green) displacements (top-left) and related spectra of the accelerometers (bottom-left). For a better display, the spectrum of the vertical component is shifted a factor 10 down and the one of the radial component is shifted a factor 10 up. The grey dashed lines show the low, intermediate and high frequency asymptotes, respectively. The low and high corner frequencies follow from the two intersections of the asymptotes.
Quotient of spectra Q (top-right) and apparent source time functions $\dot{f}_{app}(t)$ from the accelerometer (bottom-right).

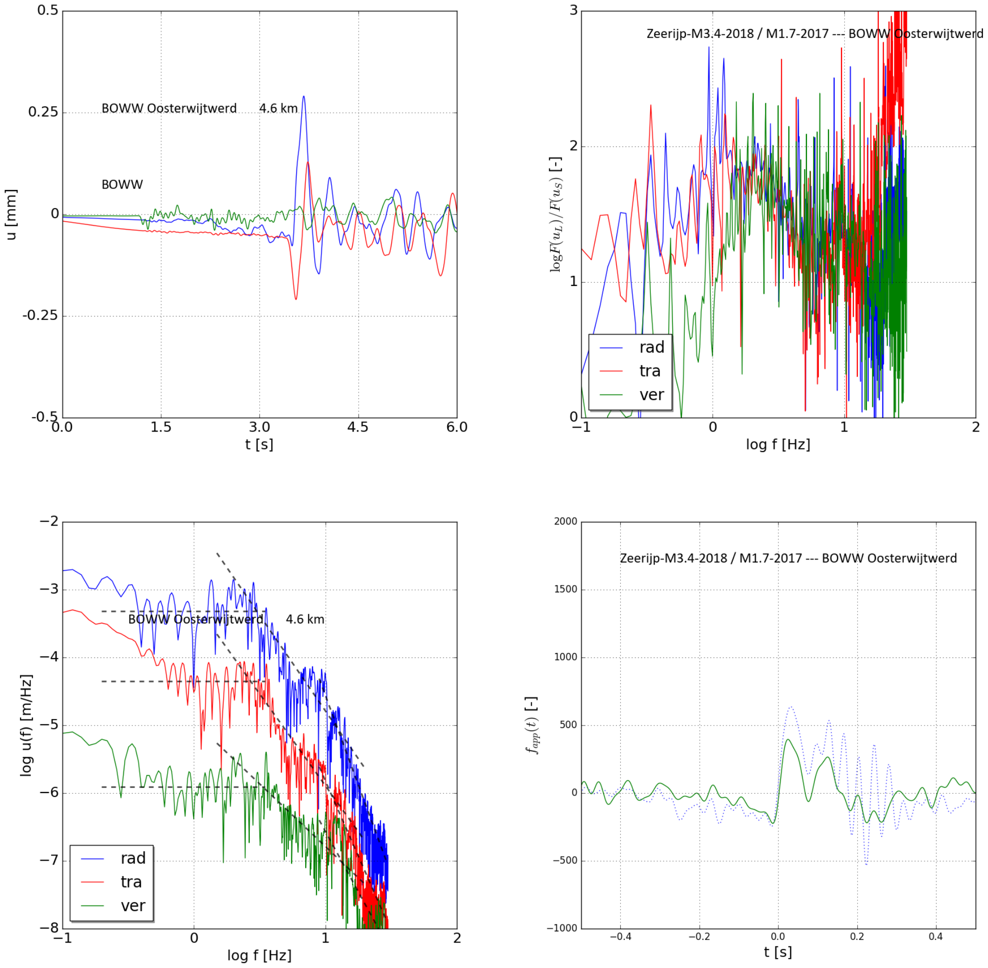

Figure B.14 : Station BOWW: radial (blue), transverse (red) and vertical (green) displacements (top-left) and related spectra of the accelerometers (bottom-left). For a better display, the spectrum of the vertical component is shifted a factor 10 down and the one of the radial component is shifted a factor 10 up. The grey dashed lines show the low, intermediate and high frequency asymptotes, respectively. The low and high corner frequencies follow from the two intersections of the asymptotes.
Quotient of spectra Q (top-right) and apparent source time functions $\dot{f}_{app}(t)$ from the accelerometer (bottom-right).

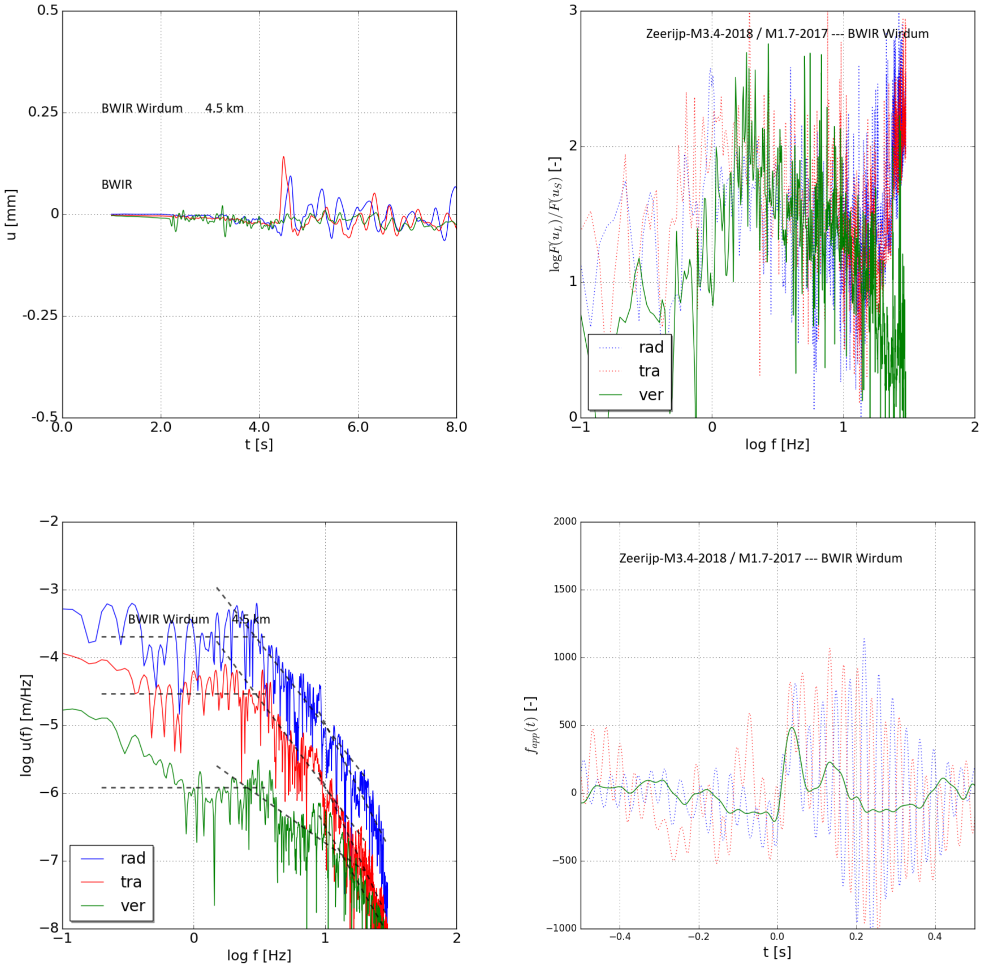

Figure B.15 : Station BWIR: radial (blue), transverse (red) and vertical (green) displacements (top-left) and related spectra of the accelerometers (bottom-left). For a better display, the spectrum of the vertical component is shifted a factor 10 down and the one of the radial component is shifted a factor 10 up. The grey dashed lines show the low, intermediate and high frequency asymptotes, respectively. The low and high corner frequencies follow from the two intersections of the asymptotes.
Quotient of spectra Q (top-right) and apparent source time functions $\dot{f}_{app}(t)$ from the accelerometer (bottom-right).

Appendix B.2 Corner frequencies

Figure B.16 shows the average displacement spectra of the ground accelerometers and geophones within a distance of about 8 km from the tremor epicentre, see also Figure 2.1 . The accelerometer and geophones signals have been filtered in the frequency domain with a 2^{nd} order high pass filter with cut-off frequencies of 0.2 Hz and 1 Hz, respectively. The filters suppress the low-frequency electronic disturbances[2].

When averaging, the spectrum of each signal has been normalised by dividing it by the integral of its spectrum. Herewith, spectra of weaker signals from seismometers farther away from the tremor epicentre contribute similar to the average as the spectra of stronger signals from seismometers close to the tremor epicentre.

To the eye, the average log-log spectra indicate two slopes and two corner frequencies. This shape of the spectrum is frequently observed for non-equidimensional rupture planes of natural earthquakes and could be understood from kinematic models, see Appendix D, §D.3.

The displacement spectra of the ground accelerometers and geophones show a more or less pronounced bump in the spectra around 10 Hz. This bump appears somewhat stronger in the spectra of the geophones. In the spectra of the individual stations, shown in Figures B.1 - B.15 , this bump can be quite prominent.

Presumably, this modification of the amplitude spectrum, pending on the frequency and source-receiver azimuth angle ϕ_s, originates from the kinetics of a rupture process along fault strike, consistent with Eqs. (D.3.7) and (D.3.8) for uni- and bi-directional rupture propagation along fault strike.

The low and high corner frequencies are defined by the intersections of the asymptotes. The derivation of the asymptotes depends on subjective choices, made for the lower and upper frequency bounds for the asymptotes, f^- and f^+. Ignoring electronic low frequency noise or drift and a more or less strong peak in the spectrum around 12 Hz, we used for all signals the same frequency boundaries f^- and f^+ and derived the asymptotes from a least square error fit to the log-log spectra within these bounds.

The lower and upper frequency bounds for the horizontal asymptote are $f^- = 0.2$ Hz and $f^+ = 3.5$ Hz. For the intermediate asymptote, $f^- = 1.5$ Hz and $f^+ = 20$ Hz. For the high-frequency asymptote, $f^- = 9.0$ Hz and $f^+ = 29$ Hz.

Table B.1 gives the average values for the low and high corner-frequencies, the powers of the slopes of the asymptotes for the ground accelerometers and the geophones. Figures B.17 and B.18 show the low and high corner frequencies and the powers of the asymptotes as a function of the source-receiver azimuth angle ϕ_s. The grey dashed line in Figure B.17 is a sinus function fit to all data using a least square error method. The

---

[2] The Fourier transform in the complex plane is done in the frequency range (-30, 30 Hz with frequency steps of 0.02 Hz.

periodicity is assumed 360° when plotted versus the source-receiver azimuth angle ϕ_s. The two fit parameters are the amplitude and the phase of the sinus function.

The average high corner frequency is $\sim$ 12 Hz, see Figure B.17 [3]. It is unlikely that the derived high corner frequency relates to the rupture propagation in fault dip direction. According Savage's model, see Appendix D, §D.3, Eq. (D.3.4), the width of the slip plane along fault dip W [m] is $W \sim 4.6V_r/(2\pi f_c^s)$. Taking $V_r = 2$ km/s (90% of the S wave velocity), the width of the rupture plane would be $W \sim 0.13$ km.
This size is quite small compared to the reservoir thickness and also small compared to rupture plane dimensions expected for the release of the seismic energy of the Zeerijp tremor. In addition, recent dynamic rupture modelling of this tremor indicates that the mean rupture propagation velocity would even be lower if the slip would start at one or two nucleation sites along fault dip and, likely, a larger part of the fault plane along fault dip would have slipped, see Wentinck (2018a).

The average low corner frequency f_c^s of these spectra, as derived from the ground accelerometers, is $\sim$ 3 Hz. This value is somewhat higher for the geophones[4].

For an equi-dimensional slip plane with the nucleation of the rupture in the centre of this plane and for $V_r \sim 0.9V_s$, the equivalent radius of the slip plane R is about $R \sim 2V_s/(2\pi f_c^s)$, according to Eq. (D.3.3) in Appendix D. Taking $V_r = 2$ km/s and $f_c^s = 3$ Hz, we obtain $R \sim 0.2$ km.
Taking $R \sim W/2$ where W [m] is the width of the fault plane along fault dip, W is comparable with the reservoir thickness[5]. It is unlikely that the rupture plane has a large L/W ratio. L [m] is the length of the slip plane along fault strike.

From the variation of the duration of the apparent source time functions with the cosinus of the angle θ between the fault strike and the line from the tremor hypocentre to the receiver, $\cos\theta$, we conclude that rupture propagation along fault strike is predominantly uni-directional, see §B.3 below. From the variation of the corner frequency with ϕ_s, the rupture velocity along fault strike can be estimated. We derive $V_{r,strike} \sim 0.5V_s$, i.e., $V_{r,strike} \sim 1$ km/s.
For uni-directional rupture propagation, an upper limit for the length of the slip plane along fault strike L [m] follows from $L = V_{r,strike}\Delta t$ where Δt is the period for which $\dot{f}_{app}(t)$ is significant. For $V_{r,strike} \sim 1$ km/s and a mean value of $\Delta t \sim 0.2$ s, we have $L \sim 0.2$ km. For these values, the modified displacement spectra show the first bump in the

---

[3] Note that the calculation of this value is influenced by the bump in the displacement spectra around this frequency.

[4] The asymptote fits of geophone spectra are influenced by the more pronounced bump in the spectra around 12 Hz. Also, the geophone signals have been corrected for the response function of the geophone and filtered by a high band pass filter with a higher cut-off frequency to suppress the low frequency disturbances.

[5] A similar conclusion would follow from Eq. (D.3.6) if $f_c^s = 3$ Hz would be regarded as the high corner frequency in Savage's model.

same frequency range as observed, see Figure D.2 , top figure in Appendix D.

The estimation of $V_{r,strike}$ from the variation of the corner frequency with ϕ_s can be erroneous when the minimum value of the corner frequency would follow from the kinetics of the rupture propagation along fault dip and not from rupture propagation along fault strike. For an upper limit $V_{r,strike} \sim 0.9V_s \sim 2$ km/s, $L \sim 0.4$ km. Taking that the width of the slip plane W is comparable with the reservoir thickness, i.e., 0.27 km, the values suggest that the rupture plane is not much elongated along fault strike. Rather, it seems more or less equi-dimensional with a largest dimension L in the range 0.2 - 0.4 km.

Table B.1 : Low and high corner frequencies f_c and powers n of asymptotes as derived from the asymptotes of the average spectra of the radial, transverse and vertical displacements of the ground accelerometers and the geophones.

	$f_{c,rad}$ Hz	$f_{c,tra}$ Hz	$f_{c,ver}$ Hz	n_{rad} -	n_{tra} -	n_{ver} -
low corner frequency						
- accelerometer	3.0	2.9	3.0	-2.2	-2.0	-1.3
- geophones	3.3	3.9	2.4	-1.6	-1.6	-1.7
high corner frequency						
- accelerometer	12.2	12.3	12.9	-4.0	-3.7	-3.1
- geophones	13.8	13.7	14.4	-4.5	-4.6	-4.7

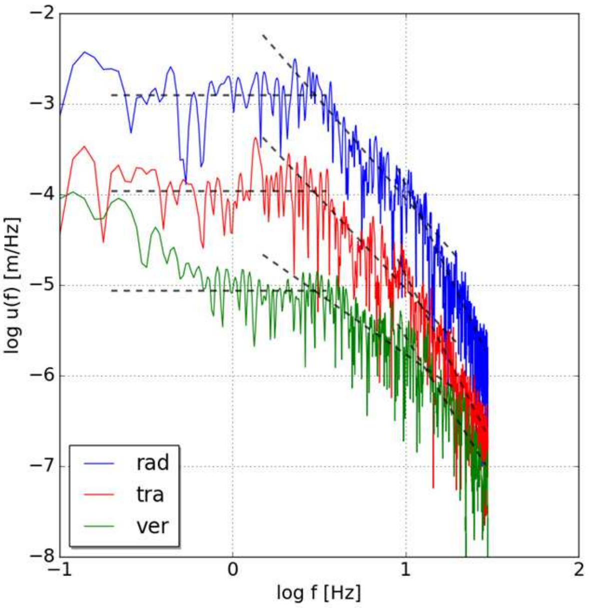

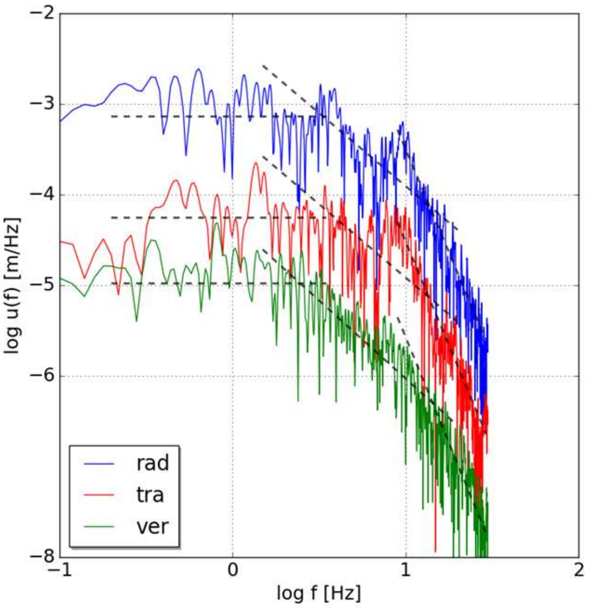

Figure B.16 : Average spectra of the displacement components recorded by ground accelerometers (top figure) and geophones (bottom figure) of the B and G stations around the Zeerijp tremor epicentre. The locations of the stations are shown in Figure 2.1 . The average spectra are for the radial (blue), transverse (red) and vertical (green) displacement components. The average includes the signals of all geophones at 50, 100, 150 and 200 m depth.

The spectra of the radial and transverse components primarily follow from the S wave, the spectrum of the vertical component primarily follows from the P wave. For a better display, the spectrum of the vertical component is shifted a factor 10 down and the one of the radial component is shifted a factor 10 up. The grey dashed lines are the asymptotes following from a least square error fit. They are used to determine the corner frequencies from intersections. For the radial, transverse and vertical components they are 3.0, 2.9 and 3.0 Hz, respectively. For $f > f_c^s$, the asymptotes $\propto f^{-n}$ with $n \sim 2$ for the radial and transverse components and $n \sim 1.3$ for the vertical component.

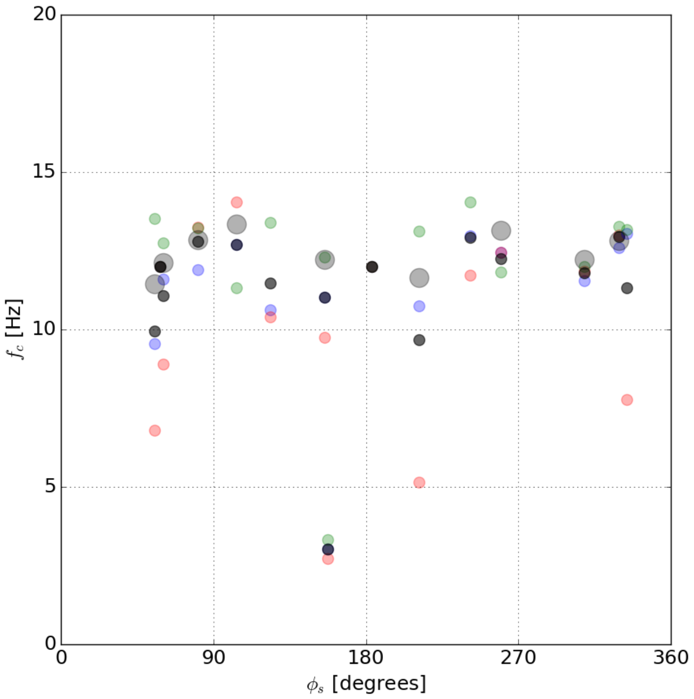

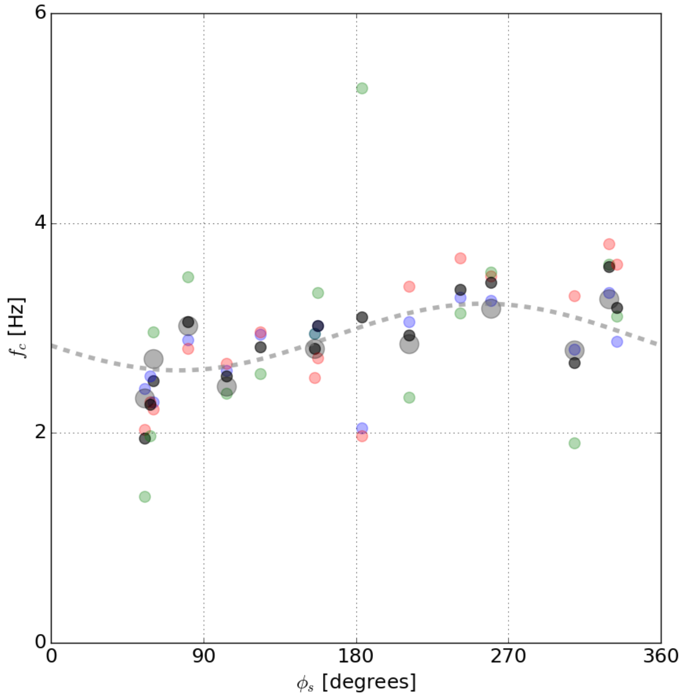

Figure B.17 : High and low corner frequencies as a function of the source-receiver azimuth angle using the ground accelerometer data of all B and G stations except station BZN1. Top figure: high corner frequency. Bottom figure: low corner frequency.
The blue, red and green dots are from the radial, transverse and vertical components. The small black dots are the average of these components. The large grey dots are averages including the data from the geophones. The grey dashed line is a sinus function least square error fit to all data with an assumed periodicity of 360°.

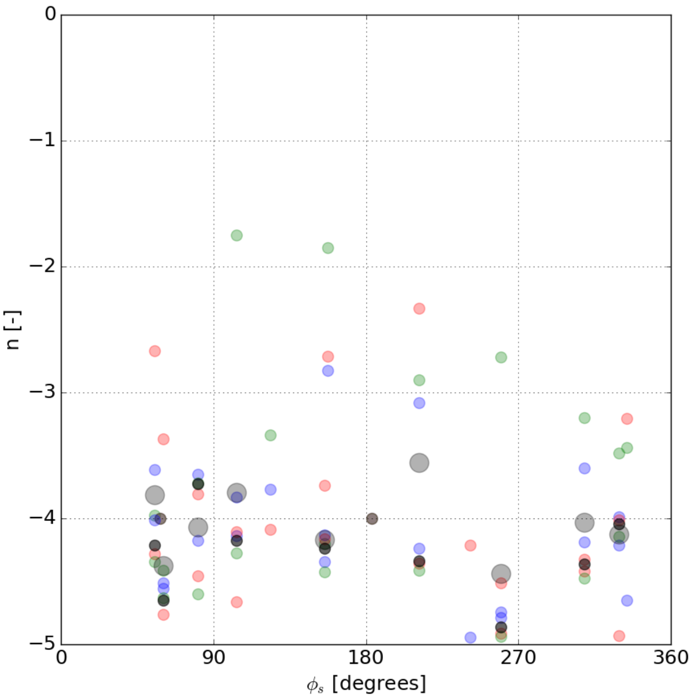

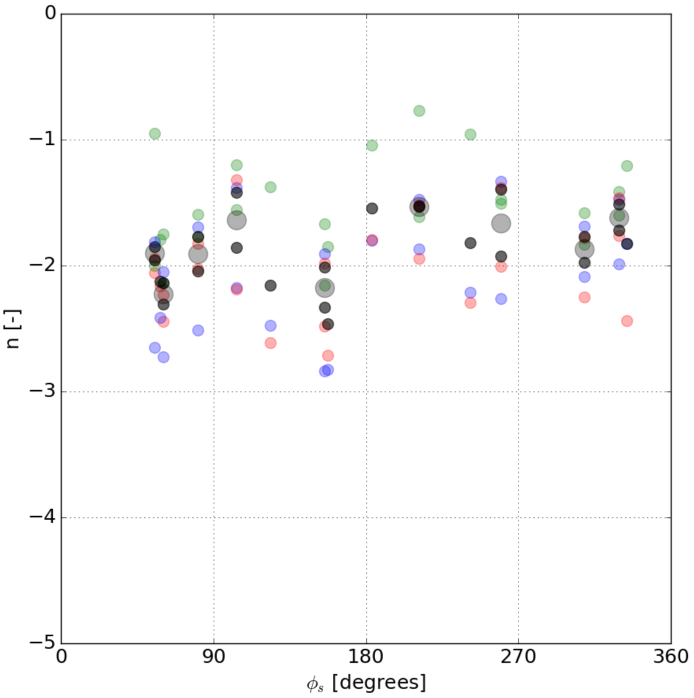

Figure B.18 : Powers of the intermediate and high frequency asymptotes as a function of the source-receiver azimuth angle using the ground accelerometer data of all B and G stations except station BZN1. Top figure: power of high frequency asymptote. Bottom figure: power of intermediate frequency asymptote.
The blue, red and green dots are from the radial, transverse and vertical components. The small black dots are the average of these components. The large grey dots are averages including the data from the geophones.

Appendix B.3 Apparent source time function from empirical Green functions

Of all small tremors with a hypocentre close to the hypocentre of the Zeerijp $\mathrm{M_L}$ 3.4 tremor, the $\mathrm{M_L}$ 1.7 tremor of December 22 in 2017, has a similar focal mechanism as the $\mathrm{M_L}$ 3.4 tremor. Using the observed displacements from the $\mathrm{M_L}$ 1.7 tremor, we have derived the apparent source time functions of the $\mathrm{M_L}$ 3.4 tremor using the method of empirical Green functions (EGFs).

The idea behind the method of empirical Green functions is that the source time function $f_S(t)$ of a small tremor can be regarded as a delta type function when compared to the source time function $f_L(t)$ of a large tremor. Hence, the recorded displacements of the small tremor can be regarded as Green functions which convolute the source time function of the large tremor into the observed displacements of the large tremor, see for example Udias et al. (2014), §6.5[6].

The method fails when applying it for other small tremors close to the $\mathrm{M_L}$ 3.4 tremor hypocentre. In this respect, the occurrence of the $\mathrm{M_L}$ 1.7 tremor was a fortunate coincidence.

After calculating the Fourier transforms of the displacements of the large and the small tremors, the apparent source time function $\dot{f}_{app}(t)$ follows from

$$\dot{f}_{app}(t) = F^{-1}[Q(\omega)] \quad \text{where} \quad Q(\omega) = \frac{F[u_L(t)]}{F[u_S(t)]}. \tag{B.3.1}$$

$F[u_L(t)]$ and $F[u_S(t)]$ are the Fourier transforms of the displacements of the large Zeerijp $\mathrm{M_L}$ 3.4 and small Zeerijp M_S 1.7 tremors and F^{-1} stands for the inverse Fourier transformation. ω [rad/s] is the circular or angular frequency, i.e., $\omega = 2\pi f$. The displacement signals used are from a period of about 13 s during the passage of the P and S waves. The signals have been additionally filtered by a 2^{nd} order band pass filter between 1 and 20 Hz. The Fourier transforms are over a range -30, 30 Hz with a frequency step of 0.02 Hz. The calculations have been done for the ground accelerometers and geophones and for all components.

Figures B.1 - B.14 in §B.1 show the apparent source time functions on the right side of these figures. They are based on the ground accelerometer signals and the mean of the signals from the four geophones at 50, 100, 150 and 200 m depth.

In general, the source time functions of the accelerometers and geophones compare well which gives confidence to the results obtained. The apparent source time functions of a few components are missing because the signals had considerable electronic disturbances,

---

[6] Note that the source time function of the small $\mathrm{M_L}$ 1.7 tremor is not a pure $\delta(t)$ function.

interfering with the Fourier transforms taken[7].

Figure B.19 shows the duration Δt_{50} [s] of the apparent source time functions versus the source-receiver azimuth angle ϕ_s and versus the cosinus of the angle θ between the fault strike and the line from the tremor hypocentre to the receiver, $\cos\theta$[8].
Δt_{50} is defined as the period in which $\dot{f}_{app}(t)$ exceeds 50% of the maximum value. From this variation the dimensions of the slip plane can be estimated, see Appendix D, §D.3. The grey dashed line is sinus function fit to all data with preset periodicity of 360°. Important is that $\dot{f}_{app}(t)$ is not symmetric around $\cos\theta = 0$. For a bi-directional rupture, the plot would be symmetric around $\cos\theta = 0$, according to Eq. (D.3.11) in Appendix D. We conclude that the rupture propagation along fault strike is predominantly uni-directional. This is consistent with a periodicity of 360° for the fit to $\dot{f}_{app}(t)$.

The duration of the apparent source time function is relatively short (or Δt_{50} is minimal) for a source-receiver azimuth angle $\phi_s \sim 300°$. This fairly well agrees with a maximum low corner frequency f_c at $\phi_s \sim 250°$ regarding uncertainties in determining f_c, see the fit function in Figure B.17 . This indicates that the rupture proceeds along fault strike in north direction.
Figure B.20 shows how a few typical source time functions shapes are distributed over the map around the Zeerijp tremor epicentre. The sharply shaped source time functions are more to the north of the tremor epicentre. The broader ones with a double peak are more to the south of the tremor epicentre.
The mean $\Delta t_{50} \sim 0.1$ s. Assuming a Gaussian shaped source time function with a standard deviation of about 0.1 s, the corresponding corner frequency would be about 3 Hz[9] which fairly well agrees with the observed mean low corner frequency of the spectra.

The variation in Δt_{50} is about 50% of the mean value. For uni-directional rupture propagation along fault strike, according to Eq. (D.3.7) in Appendix D, this means $V_s/V_r \sim 2$ and the rupture velocity along fault strike is about 50% of the S wave velocity in the reservoir or about 1 km/s.

---

[7] So, for stations BLOP and BOWW, the transverse component is missing, for station BZN1 the vertical component is missing and for station BWIR the radial and transverse components are missing. For a few stations, signal filtering was done in the time domain instead of in the frequency domain.

[8] Note that in this figure Δt_{50} is plotted versus $\cos\theta = \sin i \cos(\phi_s - \phi)$ and not versus θ. i is the take-off angle of the ray from the source to the receiver. The take-off angle is the angle between the zenith (or positive vertical) and the line from the seismic source to the receiver. ϕ is the strike azimuth angle of the fault and ϕ_s is the source-receiver azimuth angle, see Appendix D, §D.3.

[9] For a triangular and a rectangular shaped source time function with a base of 0.2 s, the corner frequency would be about 3.8 and 2.1 Hz, respectively

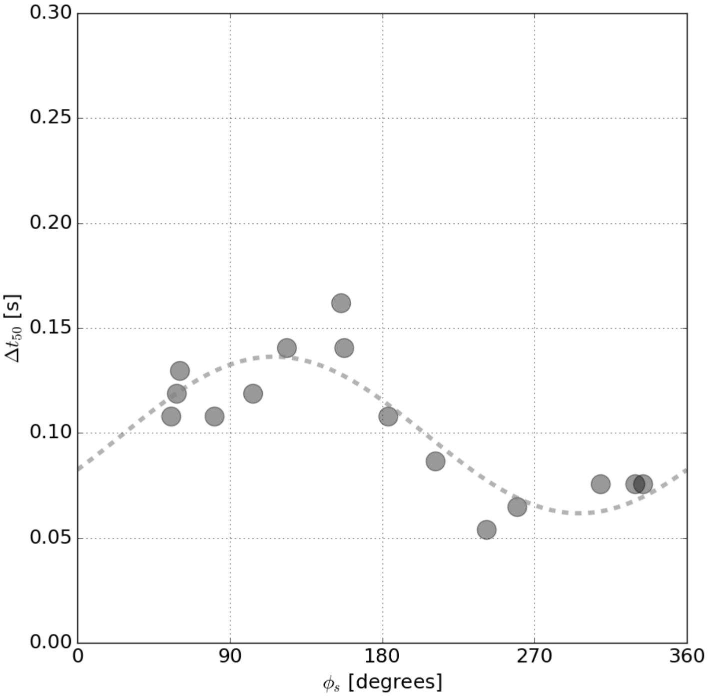

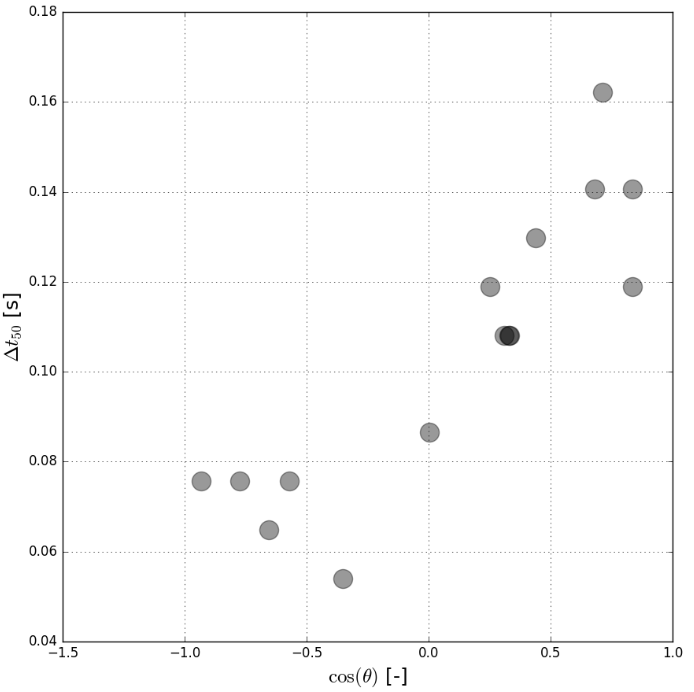

Figure B.19 : Duration Δt_{50} [s] of the apparent source time functions versus the source-receiver azimuth angle ϕ_s (top) and the cosinus of the angle θ between the fault strike and the line from the tremor hypocentre to the receiver, $\cos(\theta)$ (bottom).
The grey dashed line is a sinus function fit to all data with a preset periodicity of 360° for $\dot{f}_{app}(t)$ versus ϕ_s. Important is that $\dot{f}_{app}(t)$ is not symmetric around $\theta = 0$. For a bi-directional rupture, the plot would be symmetric according to Eq. (D.3.11) in Appendix D. We conclude that the rupture propagation along fault strike is predominantly uni-directional. This is also in agreement with a periodicity of 360° for the fit to $\dot{f}_{app}(t)$.

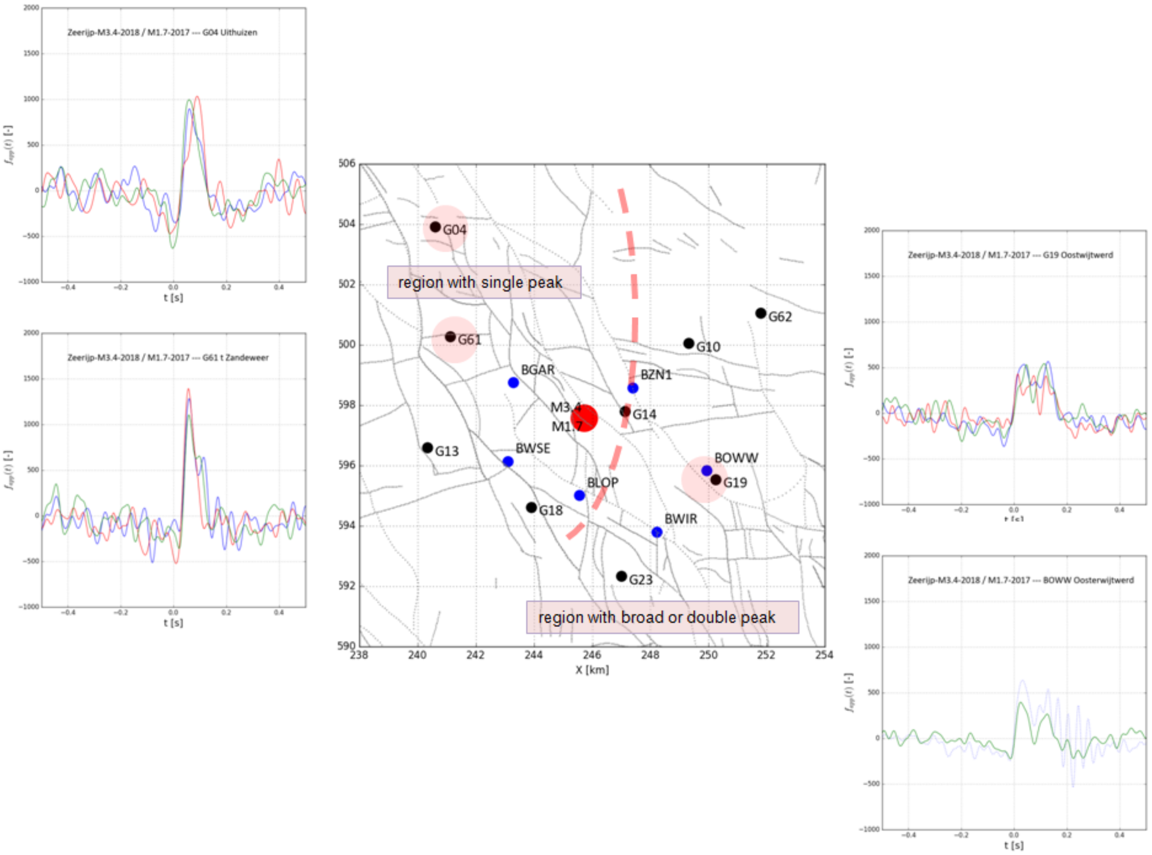

Figure B.20 : Distribution of typical apparent source time functions around the Zeerijp tremor epicentre (red dot) illustrated by these functions at stations G04, G61, G19 and BOWW. Sharply shaped source time functions are more to the north west of the Zeerijp tremor epicentre. The broader ones with a double peak are more to the south east of the tremor epicentre. It could be that in the north west the two peaks merge to form a single peak. The dashed line in the map separates the stations which recorded the single peak from the stations which recorded the single peak.

Appendix B.4 P and S wave arrivals times

In general, displacements peak when the P and S waves pass the ground accelerometers. The time differences between the observed peaks can be used to estimate the depth of the tremor hypocentre. For the Zeerijp tremor, the hypocentre depth of 2950 m has been determined by Ewoud van Dedem (SGS-I) and Bernard Dost (KNMI) from moment tensor inversion techniques.

This calculation is consistent with travel times of P and S waves obtained from ray tracing for a point source using a simplified velocity model of the subsurface. Ray tracing is based on standard wave refraction equations for elastic waves passing flat interfaces between rocks with different elastic properties. These include mode conversions from P to S and from S to P waves and the related refraction angles and transmission coefficients, see for example Aki and Richards (2009), §5.2.4. The equations are particularly useful for waves with wavelengths significantly smaller than the thickness of the formations through which the waves propagate.

The simplified velocity model used for the ray tracing calculations has five subsurface formations I-V, see Table B.2 and Figure A.1 . The mean P wave velocity $V_{p,mean,II}$ [m/s] in formation II is calculated from $V_{p,mean,II} = \sum h_{mean,i} / \sum (h_{mean,i}/V_{p,mean,i})$. Herein, $h_{mean,i}$ [m] and $V_{p,mean,i}$ [m/s] are the mean thickness and the mean P wave velocity in formation i, respectively. The summation is over all subsurface formations in formation II, i.e., the anhydrite, lower Zechstein, floater and upper Zechstein formations. $V_{p,mean,i}$ is calculated from $V_{p,mean,i} = h^{-1}_{mean,i} \int V_p^{-1}(z)dz$ where the integration is over the depth of formation i. Similar equations apply for formations II and V and for the S wave velocities in these formations.

Figure B.21 shows the calculated arrival times from ray tracing, FEM simulations and the difference between the observed arrival times for the calculated, simulated and observed waves. We correct the simulated arrival times from FEM simulations for a time delay of 0.1 s caused by the generation time of the tremor in the simulation and the calculated and simulated arrival times from ray tracing and FEM simulations for a delay in arrival time of the S wave at surface because of wave slow down in shallow subsurface. As expected, the simulated time difference Δt_{PS} between the peaks in the signals indicating the passage of P and S waves fairly well correspond with the observed time differences.

Table B.2 : Formations used in a simplified subsurface model for ray tracing calculations for the Zeerijp tremor. The depths of the lower horizons of formations I - V are equal to the mean depth of the lowest subsurface formation that is included in this formation. The mean P and S wave velocities in formations I - V are also shown by the dashed lines in Figure A.1 .

Formation	Formations included	depth lower horizon m	$V_{p,mean}$ m/s	$V_{s,mean}$ m/s
V	Upper North Sea Lower North Sea	-810	2028	682
IV	Chalk	-1700	3460	1659
III	Rijnland Altena Triassic	-1965	3402	1868
II	upper Zechstein floater lower Zechstein anhydrite	-2852	4530	3402
I	Rotliegend reservoir	-3120	3800	2232

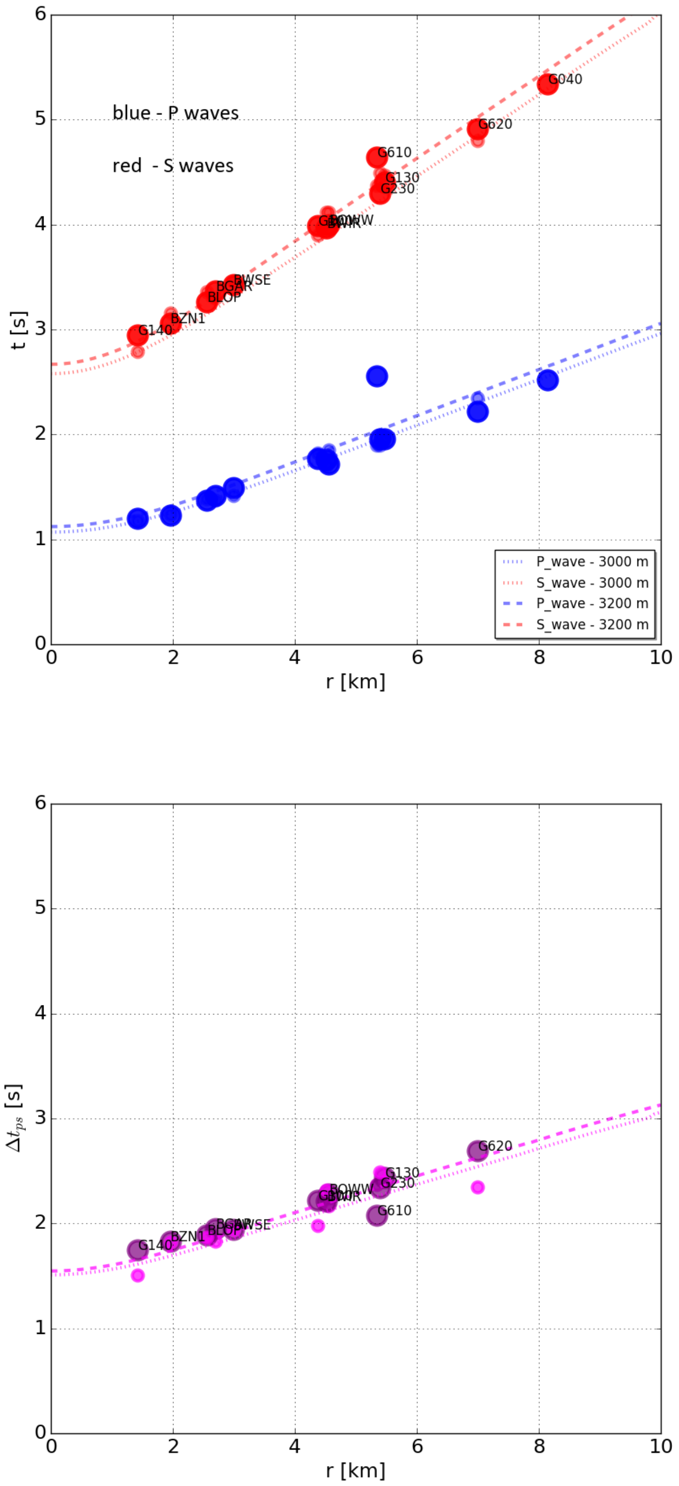

Figure B.21 : Left: arrival times of P and S waves according to FEM simulations (dots) and according to ray tracing (dotted and dashed lines) as a function of distance from the tremor epicentre r [m] for two hypocentres at 3 km and 3.2 km depth, respectively. Right: simulated, calculated and observed time difference Δt_{PS} as a function of the distance from the tremor epicentre. The large purple dots show the observed time differences at the station locations. The dotted and dashed lines follow from ray tracing.

Appendix B.5 Response functions accelerometers and geophones

The transfer or response functions of the KNMI instrumentation are expressed in terms of poles and zeros in the Laplace or frequency domain[10]. These functions are presented with the complex variable $s = i\omega$ where $\omega = 2\pi f$ is the circular frequency [rad/s] and f [Hz] is the frequency.

The transfer or response function $T(s)$ relating the output of a seismometer $\zeta(s) = T(s)u(s)$ [counts,V] to a ground motion $u(s)$ [m] has the general form

$$T(s) = \frac{\zeta(s)}{u(s)} = S\frac{\Pi_{i=1}^{k}(s - z_i)}{\Pi_{j=1}^{l}(s - p_j)}. \tag{B.5.1}$$

The ground accelerometers of the B and G stations are EpiSensor^{TM} broadband DC - 200 Hz accelerometers from Kinemetrics, Inc., CA (US)[11].

The response function of the ground accelerometer is essentially constant for frequencies of interest, i.e., below 30 Hz. At low frequencies, the combined gain of the accelerometer and data-logger is $S = 2.134\ 10^5$ counts/(m/s^2) displacement acceleration.

The geophones in the shallow boreholes are SM-6H sensors from ION (Input/Output, Inc.). Below 4.5 Hz the sensitivity decreases with f^2. According to Dost (2016), the following transfer function applies

$$T_s(s) = S\frac{s^3}{s^2 + 2h_0\omega_0 s + \omega_0^2} = S\frac{s^3}{(s - p_0)(s - p_0^*)}. \tag{B.5.2}$$

The inverse response function $T^{-1}(s)$, defined by $u(s) = T^{-1}(s)\zeta(s)$, is

$$T_s^{-1}(s) = \frac{1}{S}\frac{(s - p_0)(s - p_0^*)}{s^3}. \tag{B.5.3}$$

$S = 28.8$ V/m. $\omega_0 = 2\pi f_0$ and $f_0 = 4.5$ Hz with a damping parameter $h_0 \sim 0.71$, this results in the complex conjungate poles $p_0 =$ (-19.84,20.14j) and $p_0^* =$ (-19.84,-20.14j).

---

[10] Also, a set of equivalent recursive time-domain filters have been designed, which gives in general a more stable calculation of the ground motions than in the frequency domain. These recursive time domain transforms are based on the so-called Z-transform, see Dost and Haak (2002).

[11] The EpiSensor^{TM} accelerometer output signals follow the convention of a positive output in the direction of the orientation (X,Y) or (east,north) axis arrows on the sensor housing. One reason for very low-frequency signals is some temperature drift. Over time a 'non-zero DC-offset' can develop. According to the specifications of the EpiSensor^{TM} accelerometers, the temperature drift is 0.5 mg/°C or 5 mm/s^2/C. So, over a period of 2 seconds, the corresponding amplitude drift from a temperature change of 0.01 °C is $\sim$ 0.1 mm.

At 10 Hz, the combined gain of the geophone and data-logger is $S = 2.502\ 10^8$ counts/(m/s) displacement velocity. Figure B.22 shows the transfer or response functions used.

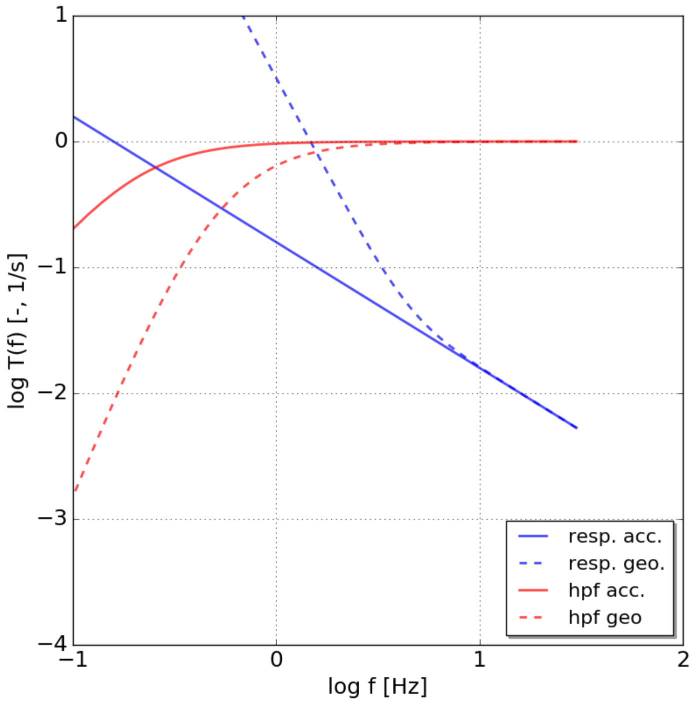

Figure B.22 : Transfer or response functions of the ground accelerometers and geophones from displacement velocities to displacements in the frequency domain.
The solid blue line is the transfer function of the ground accelerometer in the frequency domain. This function is used after the displacement accelerations have been integrated in the time domain to obtain displacement velocities. The dashed blue line is the response function used for the geophones. This function compensates for the decay in response below 4.5 Hz.
The red solid line is the high pass filter for the ground accelerometer signals. The red dashed line is the high pass filter for the geophone signals.

Appendix C

Additional simulations

Additional simulations have been done varying the rake angle (or slip direction), the length of the seismic source along fault strike, the focal mechanism and the depth of the tremor hypocentre. So far, no significant improvements have been seen for other rake angles. As expected, the displacement peaks become somewhat sharper for a smaller source length along fault strike. However, another source dimensions does not lead to a better fit of the simulations to the observed data.

Table C.1 lists the variations of the other seismic source parameters shown in Figures C.1 - C.4 . Figures C.1 and C.2 show that variations in dip angle δ and fault azimuth angle ϕ do matter but do not resolve the significant discrepancy between the observed and simulated amplitudes of stations G18, G10 and BZN1. Figures C.3 and C.4 show similar differences in displacements if the tremor hypocentre depth is 250 m deeper but also another depth do not improve the fits.

Table C.1 : Seismic source parameters varied in Figures C.1 - C.4 . These are the fault dip angle δ, the fault azimuth angle ϕ and the hypocentre depth.

	simulation	δ degree	ϕ degree	depth m
....	....	....	....	....
base case	300-105/106	67	310	2985
variation focal mechanism				
- dip angle	300-107/108	80	310	2985
- fault strike azimuth angle	320-101/102	70	297	2985
- depth	320-103/104	70	297	3235

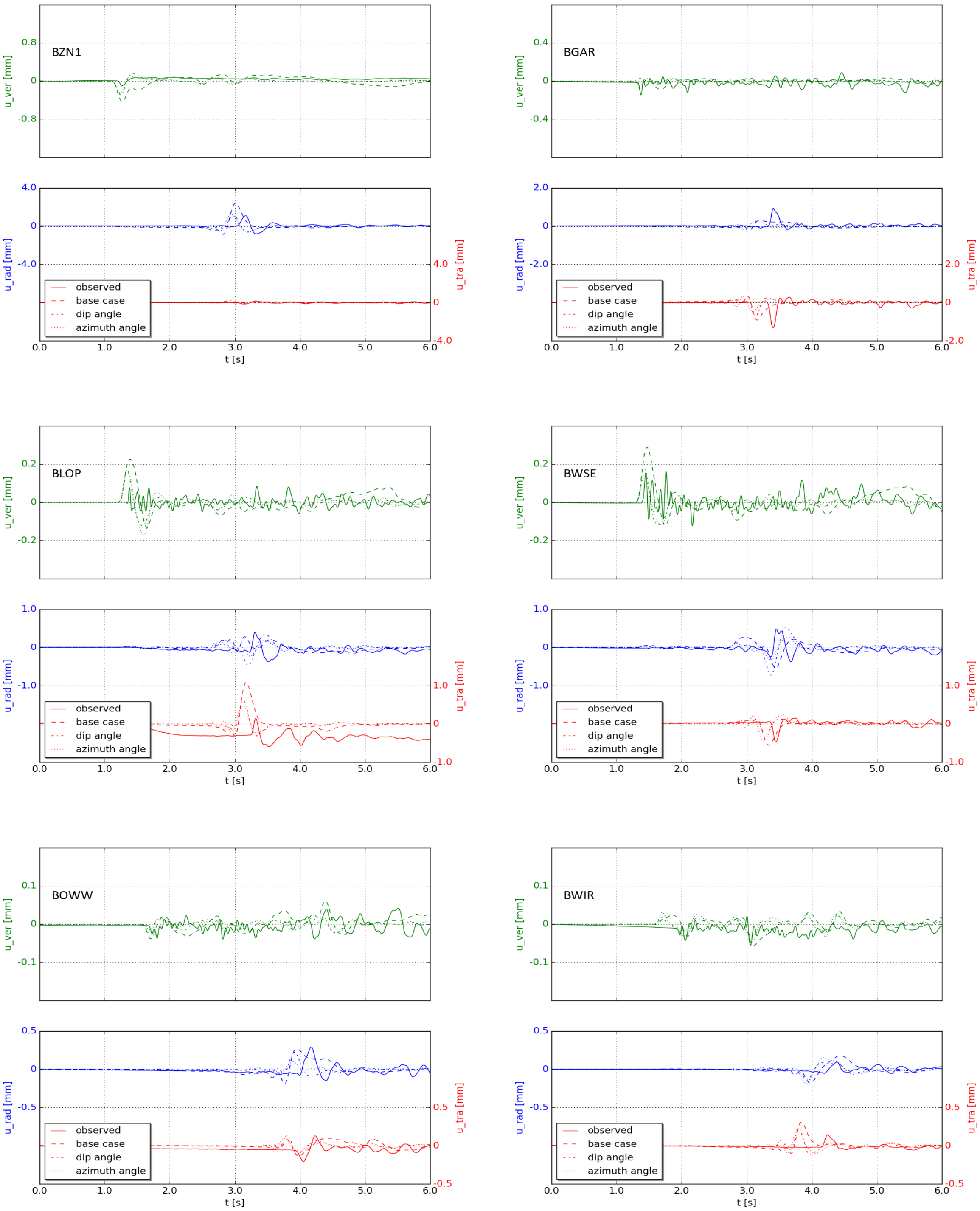

Figure C.1 : Observed (solid) and simulated (dashed) vertical (green), radial (blue) and transverse (red) displacements following from the Zeerijp M_L 3.4 tremor, recorded by the ground accelerometers of the BZN1, BGAR, BLOP, BWSE, BOWW and BWIR stations. The simulations shown are the base case (dashed), one for a dip angle of 80° (dash-dotted) and one for a fault strike azimuth angle of 297° (dotted). The simulated radial and transverse displacements have been shifted 0.2 s in time and amplified twice to include the effect of the slow down of the S wave in the shallow subsurface.

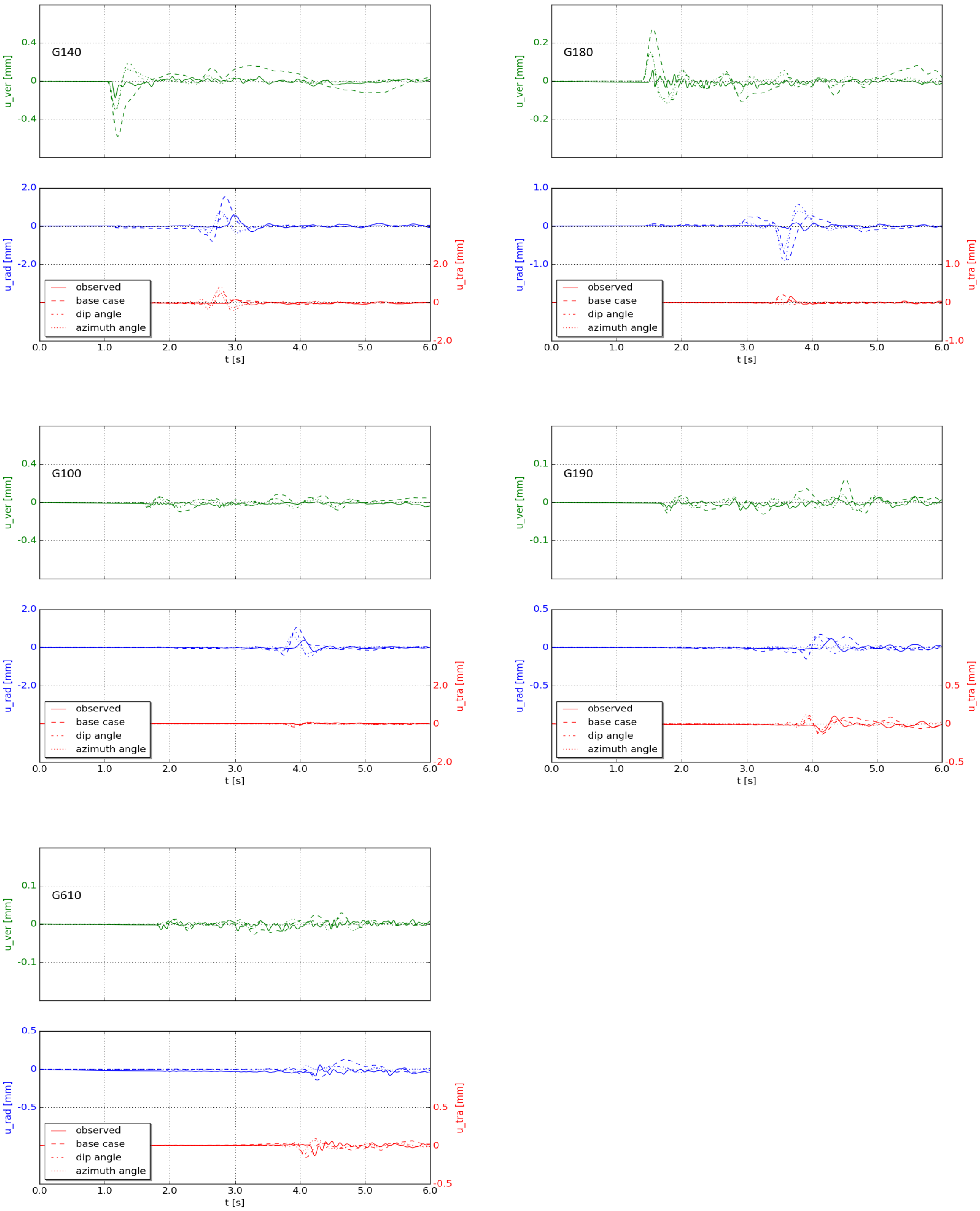

Figure C.2 : Observed (solid) and simulated (dashed), vertical (green), radial (blue) and transverse (red) displacements following from the Zeerijp M_L 3.4 tremor, recorded by the ground accelerometers of the G14, G18, G10, G19 and G61 stations.
The simulations shown are the base case (dashed), one for a dip angle of 80° (dash-dotted) and one for a fault strike azimuth angle of 297° (dotted). The simulated radial and transverse displacements have been shifted 0.2 s in time and amplified twice to include the effect of the slow down of the S wave in the shallow subsurface.

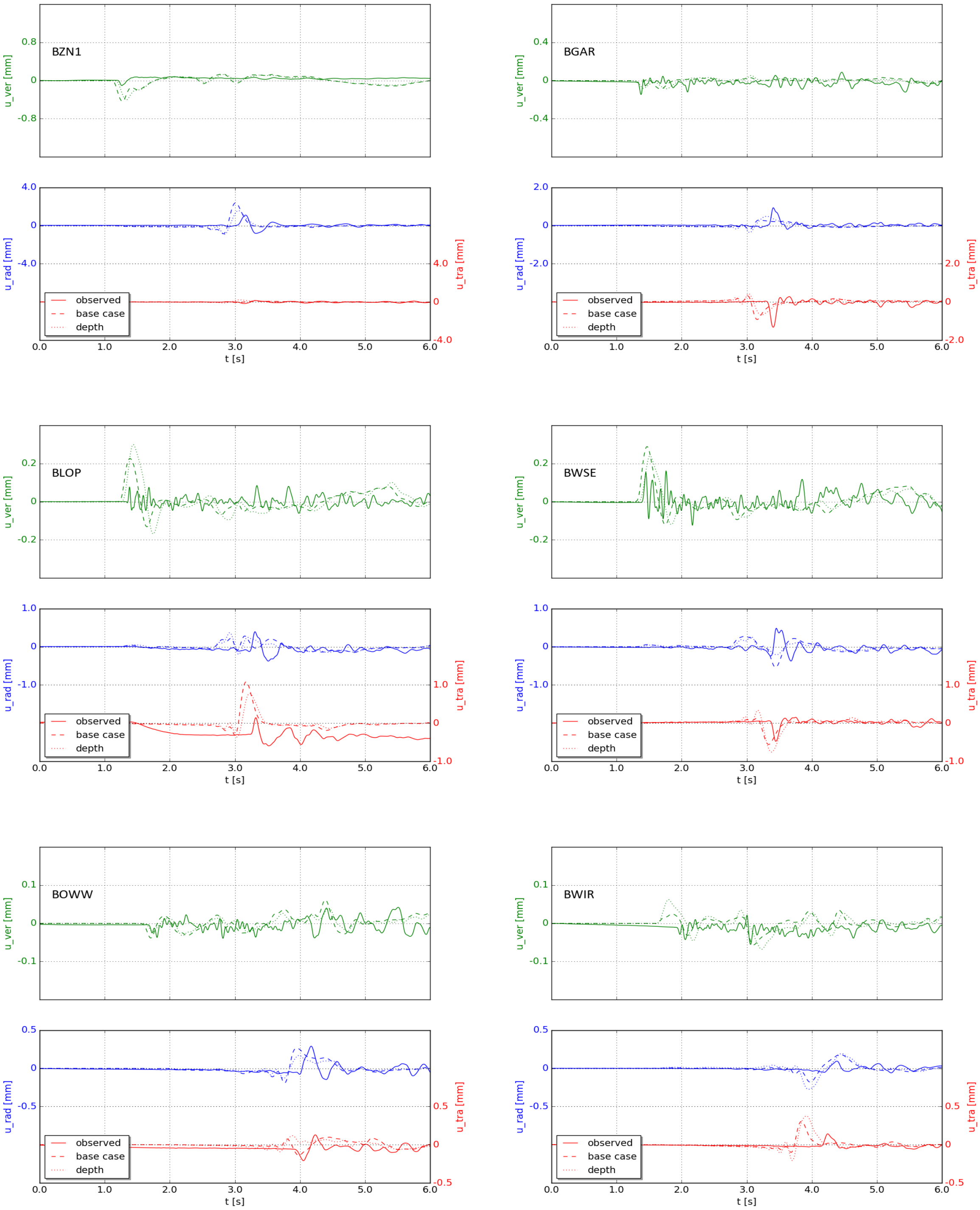

Figure C.3 : Observed (solid) and simulated (dashed) vertical (green), radial (blue) and transverse (red) displacements following from the Zeerijp M_L 3.4 tremor, recorded by the ground accelerometers of the BZN1, BGAR, BLOP, BWSE, BOWW and BWIR stations. The simulations shown are the base case (dashed) and one for a tremor hypocentre at 3235 m depth, or 250 m deeper (dotted). The simulated radial and transverse displacements have been shifted 0.2 s in time and amplified twice to include the effect of the slow down of the S wave in the shallow subsurface.

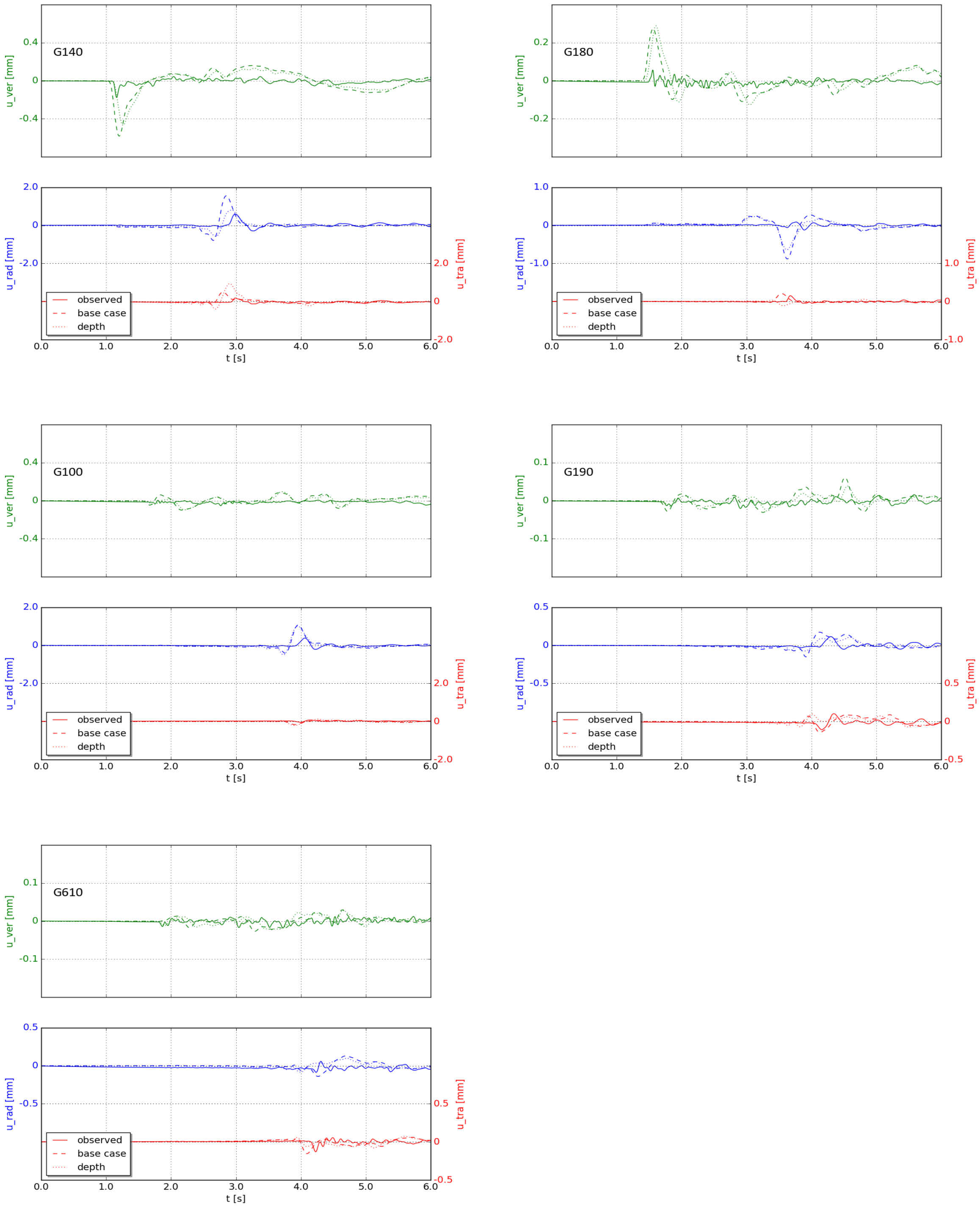

Figure C.4 : Observed (solid) and simulated (dashed), vertical (green), radial (blue) and transverse (red) displacements following from the Zeerijp M_L 3.4 tremor, recorded by the ground accelerometers of the G14, G18, G10, G19 and G61 stations.
The simulations shown are the base case (dashed) and one for a tremor hypocentre at 3235 m depth, or 250 m deeper (dotted). The simulated radial and transverse displacements have been shifted 0.2 s in time and amplified twice to include the effect of the slow down of the S wave in the shallow subsurface.

Appendix D

Seismic source

Appendix D.1 Source time functions

A seismic source can be modelled as a point source or as an extended source. For a point source, the kinematics of the rupture process is completely defined by a single so-called dimensionless source time function $f(t)$ [-]. For a point source, the dimensions of the slip plane, the slip rate and rupture velocity are indistinguishable and implicitly included in the dynamics of the source time function.

Take that the reservoir rock is uniform and isotropic and the slip is only deviatoric. For a receiver at a large distance from the seismic source, the source can be represented by a point source with a double couple or with a moment tensor[1]. The time dependent moment tensor $\boldsymbol{M} = \boldsymbol{M}(t)$ [N] can be factorised in a unit moment tensor $\boldsymbol{m}$ [-] and a source time function $M_0(t)$ [N]. The unit moment tensor $\boldsymbol{m}$ [-] is constructed from the unit vectors defining the orientation of the rupture plane and the slip direction, see e.g. Aki and Richards (2009), §3.3. So,

$$\boldsymbol{M}(t) = \boldsymbol{m}M_0(t). \tag{D.1.1}$$

Using the mean relative displacement or slip $D = D(t)$ over the slip plane as the time-dependent variable and the general relation between slip and seismic moment $M_0 = \mu SD$, the seismic moment changes with time as

$$M_0(t) = \mu SD(t) = M_0 f(t) \quad \text{where} \quad D(t) = D_{max}f(t) \quad \text{and} \quad M_0 = \mu SD_{max}. \tag{D.1.2}$$

---

[1] The source tensor provides fundamental information on the event magnitude, source geometry (e.g. possible fault plane orientations and slip directions), and partitioning among various deviatoric and isotropic motion components. If the reservoir rock is uniform and isotropic, the moment tensor and the so-called potency tensor differ only by a factor equal to the shear modulus μ, see for example Zhu and Ben-Zion (2013). One of the authors notes that, in general, it is better to use the strain-based potency tensor than the stress-based moment tensor, since the potency involves only directly observable quantities whereas the moment requires making assumptions on elastic properties at the source. In this case, this is not needed.

D_{max} [m] is the maximum value of the mean slip over the slip plane over time. S [m^2] is the surface of the slip plane and μ [Pa] the shear modulus of the rock. $f(t)$ [-] is the dimensionless source time function.

Two-dimensional dynamic rupture modelling suggests that the rupture propagation along fault dip leads to a faster decay of the source time function than Brune's source time function for a given rise time τ_r [s][2], we apply the following time derivative $\dot{f}(t) = df/dt$ of the source time function, see also Wentinck (2017) and Wentinck (2018a),

$$\dot{f}(t) = g(t)\frac{t}{\tau_r^2}\exp(-(t/\tau_r)^n) \quad \text{where} \quad g(t) = c\frac{t^2}{t^2 + t_{onset}^2}. \tag{D.1.3}$$

n [-] is a shape parameter which determines the decay time of $\dot{f}$. The function $g(t)$ ensures that $f(t)$ has a zero second order time derivative at $t = 0$, which is convenient for the numerical simulations. c [-] is a constant, so that $f \to 1$ for $t \gg \tau_r$. t_{onset} [s] is a typical time in which $g(t)$ increases from 0 to 1. Using $t_{onset} \ll \tau_r$, $g(t)$ has a minimal effect on the shape of the source time function. Figure D.1 shows the source time functions used in this report.

Appendix D.2 Extended seismic source used

For an extended source, the rupture velocity and the dimensions of the slip plane are explicitly included in the seismic source model. Usually, the slip plane is divided in a number of relative small slip patches and for each patch a unique source time function is defined. To model an extended source along fault strike, we have divided the rupture plane in a number of relatively small slip patches along fault strike. These patches are represented by a series of 13 double couples with a double couple arm $l_{DC} = 40$ m over a length L of about 0.5 km. We have assumed that the rupture starts at the tremor hypocentre and propagates bi-directional, i.e., in both directions, along fault strike.
The rupture velocity along fault strike is assumed $V_{r,strike} = 2$ km/s, which is 80 - 90% of the S wave velocity in the reservoir[3]. The external source model resembles Haskell's model for an extended seismic source, see e.g. Udias et al. (2014), §7.2 or Aki and Richards (2009), §10.1.5.

---

[2] The rise time τ_r [s] is the time in which a patch of the rupture plane achieves its maximum slip D: $\tau_r \sim D/\dot{D}$ where $\dot{D}$ [m/s] is the average slip velocity during the rupture of the patch. For $D \sim 0.1$ m and $\dot{D} \sim 1$ m/s, $\tau_r \sim 0.1$ s.

[3] The rupture velocity is the velocity with which the rupture front propagates along the fault plane. The rupture velocity essentially differs from the so-called slip velocity. The latter one is the relative velocity with which one side of the fault plane fault moves with respect to the other side of the plane. The slip velocity is usually of the order 1 m/s and is determined by the breakdown stress drop and rock inertia.

The source time function for double couple or slip patch i of the series of double couples along fault strike is, using Eq. (D.1.3),

$$\dot{f}_i(t) = g(t_i^*) \frac{t_i^*}{t_r^2} \exp(-(t_i^*/\tau_r)^n). \tag{D.2.1}$$

$t_i^* = 0$ for $t < t_{trigger,i}$ and $t_i^* = t - t_{trigger,i}$ for $t \geq t_{trigger,i}$ and the trigger time $t_{trigger,i}$ [s] is given by[4],

$$t_{trigger,i} = \frac{|\boldsymbol{\zeta}_i - \boldsymbol{\zeta}_{nucl}|}{V_{r,strike}}. \tag{D.2.2}$$

$|\boldsymbol{\zeta}_i - \boldsymbol{\zeta}_{nucl}|$ is the distance between double couple i and the tremor hypocentre where the rupture is supposed to start. $V_{r,strike}$ [m/s] is the rupture velocity along fault strike.

---

[4] With a focus on the low-frequency content of the simulated waves, we disregard possible irregularities in the rupture velocity along fault strike due to fault plane and stress heterogeneity. To include them, see for example Graves and Pitarka (2010) or Graves and Pitarka (2015).

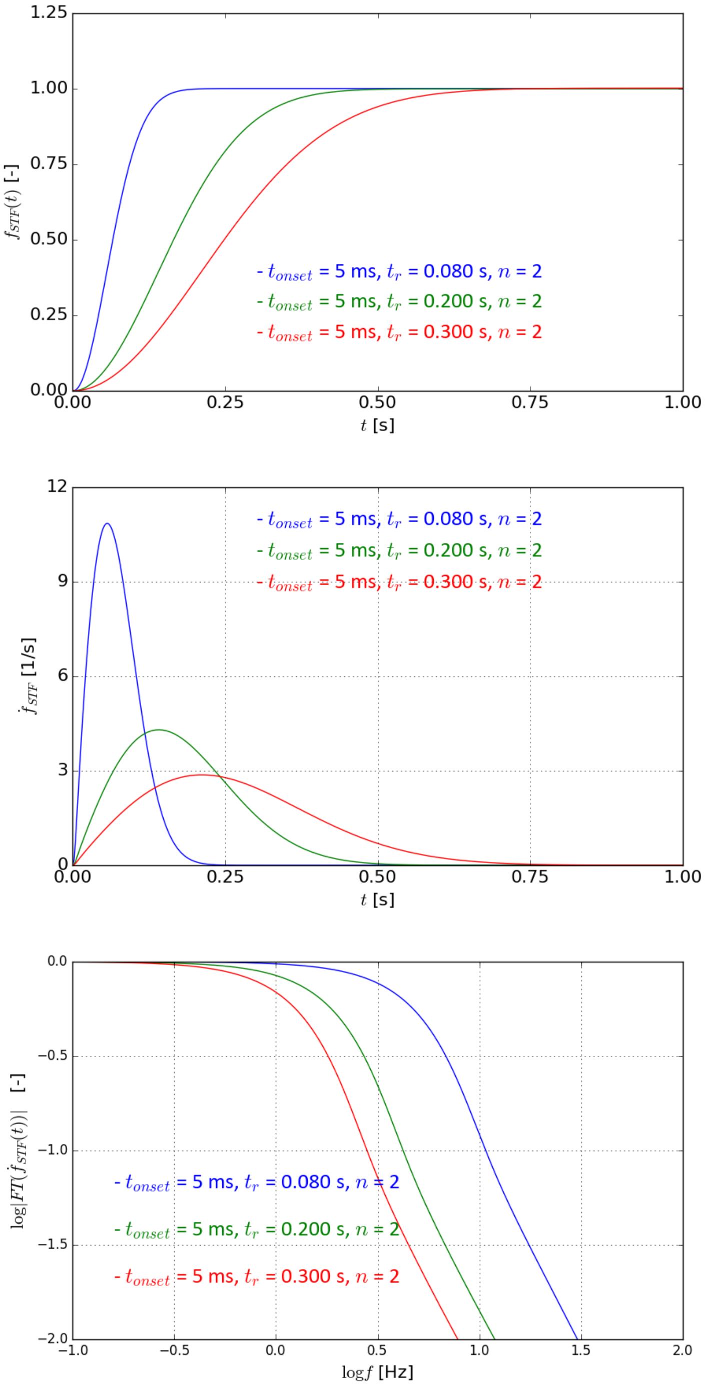

Figure D.1 : Source time function $f(t)$ (top), time derivative $\dot{f}(t)$ (centre) and absolute values of the logarithm of the Fourier transforms of the time derivative $\log^{10}|F(\dot{f}(t))|$ (bottom).

The shape parameters are $n = 2$, $t_{onset} = 5$ ms and $\tau_r = 0.08$ s (blue), 0.2 s (green) and 0.3 s (red). The corresponding corner frequencies are 5.2, 2.1 and 1.4 Hz, respectively. In all cases, the small onset time t_{onset} has a negligible effect on the shapes of the curves. For the slip patches along fault strike we use $n = 2$, $t_{onset} = 5$ ms and $\tau_r = 0.08$ s.

Appendix D.3 Slip plane dimensions and apparent source time functions

In principle, there are at least two independent time constants to be defined in a rupture process on a slip plane. The first time constant is the so-called rise time τ_r [s] in which a patch of the rupture plane achieves its maximum displacement D_{max}: $\tau_r \sim D_{max}/\dot{D}$ where $\dot{D}$ [m/s] is the average slip velocity during the slip of that patch. For a tremor like the Zeerijp tremor with magnitude M 3.4, $D_{max} \sim 0.1$ m and $\dot{D} \sim 1$ m/s, $\tau_r \sim 0.1$ s.
The second time constant t_r [s] is related to the duration of the rupture process over the entire slip plane. If L is the largest dimension of the slip plane, for an uni-directional rupture process $t_r \sim L/V_r$ where V_r [m/s] is the velocity of the rupture front propagating over the slip plane. Taking a typical value $V_r \sim 0.9V_s$, for $V_s = 2.2$ km/s and $L = 0.2$ km, $t_r \sim 0.1$ s. In this case, $\tau_r \sim t_r$ and, in practice, these characteristic times can hardly be distinguished from observations.

If the distance between the tremor epicentre and the receiver is large compared to size of the slip plane, the seismic source approximately behaves as a point source. In this case, the so-called source time function $f(t)$ [-] contains all the time dependent behaviour of the rupture process. For tremors or small-to-moderate earthquakes, this function is usually characterised by a single time constant, by definition τ_r[5]. We may consider that τ_r represents also t_r but this may not be the case. So, assuming a certain value for the rupture velocity V_r, we may not derive L from the observed displacement spectra. But, for a source time function $f(t)$ with a single dominant peak, the duration of the source time function may give an upper limit for L.

There are several relations in the literature between the dimensions of the rupture plane (or slip plane) and the corner frequencies observed in the displacement spectra of the seismometer stations around the tremor epicentre. Applying Brune's source time function, for an equi-dimensional circular slip plane with the nucleation in the centre of the slip plane, according to Udias et al. (2014), Eq. 8.3,

$$R = c' \frac{V_s}{\omega_c^s}. \tag{D.3.1}$$

---

[5] For an equi-dimensional slip plane, the inverse of the rise time τ_r of the source time function relates to ω_c as $\tau_r \sim 1/\omega_c$, see Udias et al. (2014), §4.9.

For Brune's model, the far field displacement function for the S waves can be expressed by $f(t) \propto t'/\tau_r \exp(-t'/\tau_r)$ and $t' = t - r/V_s$ and r [m] is the distance between the tremor hypocentre and the receiver, see this reference, §9.5.
The time that this function exceeds 50% of its maximum value $\Delta t_{50} \sim 3\tau_r$, see this reference §4.9, Fig. 4.16. For a triangular source time function, $\Delta t_{50} \sim \tau_r$. So, the shape of the source time function is relevant in this respect.

$\omega_c^s = 2\pi f_c^s$ [rad/s] is the angular corner frequency and f_c^s [Hz] is the corner frequency derived from the S wave and $c' \sim 2.3$ is a constant[6]. According to Aki and Richards (2009), Eq. 10.35, the constant c' is a function of the rupture velocity V_r and in the range 1.53 - 1.85. For $V_r = 0.9V_s$, $c' \sim 1.8$.

For a rectangular slip plane, according to Udias et al. (2014), Eq. 8.6 or Aki and Richards (2009), Eq. 10.33[7]

$$\sqrt{LW} = \sqrt{14.8}\frac{V_s}{\omega_c^s} \sim 3.8\frac{V_s}{\omega_c^s}. \tag{D.3.2}$$

For a square slip plane with a slip area equal to a circular one with radius R, using $W = L$ and $W^2 = \pi R^2$,

$$R = c'\frac{V_s}{\omega_c^s} \quad \text{where} \quad c' = \sqrt{\frac{14.8}{\pi}} \sim 2.1. \tag{D.3.3}$$

So, for an circular slip plane, we could use a value $c' \sim 2$.

With a number of stations around the tremor epicentre, we may observe variations in the displacement spectra and corner frequencies for different stations, depending on the source-receiver azimuth angle ϕ_s [degrees][8].
This variation could be an indication for an extended source, in particular for an elongated slip plane with a considerable aspect ratio L/W. Often, two corner frequencies can be observed in the displacement spectra: a low one and a high one. The interpretation of the corner frequencies is different for slip in one direction along fault strike, or uni-directional slip where the nucleation starts at one side of the slip plane, and for slip in two directions along fault strike, or bi-directional slip where the nucleation starts in the centre of the slip plane.

For bi-directional slip, according to Savage (1972), see also Udias et al. (2014), Eqs. 7.37 and 7.38, the high corner frequency depends on the width of the fault along dip W as,

$$\omega_c^s \sim 4.6\frac{V_r}{W}. \tag{D.3.4}$$

Vice-versa, for $V_r \sim 0.9\ V_s$,

$$W \sim 4.1\frac{V_s}{\omega_c^s}. \tag{D.3.5}$$

---

[6] Similar expressions hold for the P wave. For usual Poisson ratio's, the corner frequency derived from the P wave f_c^p would be lower than for the S wave. However, usually it is observed that f_c^p is higher than f_c^s.

[7] This expression originates from Savage (1972), see Aki and Richards (2009), §10.1.7. It is assumed that $V_r = 0.9V_s$ and that the rise time is equal to the travel time of the rupture front over half the fault width, i.e., $\tau_r = t_r = W/(2V_r)$. The corner frequency is the geometric mean of two corner frequencies associated with the finite rupture propagation and the rise time. For the S wave, $\omega_c^s = \sqrt{14.8}V_s/\sqrt{LW}$.

[8] ϕ_s is the angle of between the north direction and a line connecting the tremor epicentre and the station or receiver.

For the half-width of the slip plane along dip, $W/2$,

$$W/2 = c'\frac{V_s}{\omega_c^s} \quad \text{where} \quad c' \sim 1.8. \tag{D.3.6}$$

This value of the constant c' is comparable with the one used for a circular slip plane with radius $R = W/2$[9]. A similar relation holds for uni-directional slip.

The low corner frequency of the S wave as recorded by a receiver follows from the absolute value of the Fourier transforms or spectra of the far-field displacements. For uni-directional rupture propagation along fault strike, according to Udias et al. (2014), Eq. 7.20,

$$\big|u(\omega^s)\big| \propto \big|M_0(\omega^s)\omega^s\big|\bigg|\frac{\sin X}{X}\bigg| \quad \text{where} \quad X = X(\omega^s) = \frac{\omega^s L}{2V_s}\big(\cos\theta - \frac{V_s}{V_r}\big). \tag{D.3.7}$$

θ [degrees] is the angle between the fault strike and the line from the tremor hypocentre (ζ = 0) to the receiver. $\cos\theta = \sin i \cos(\phi_s - \phi)$ where i is the take-off angle of the ray from the source to the receiver. ϕ is the strike azimuth of the fault and ϕ_s is the source-receiver azimuth. Herewith, $|u(\omega^s)|$ oscillates with ϕ_s with an amplitude $(\omega^s L)/(2V_s)\sin i$. The term $|M_0(\omega^s)\omega^s|$ is proportional to the Fourier transform of the source time function of a slip patch on the rupture plane, $\dot{f}(t)$.

For bi-directional rupture propagation with the nucleation of the slip in the centre of the slip plane, according to Udias et al. (2014), Eq. 7.35,

$$\big|u(\omega^s)\big| \propto \big|M_0(\omega^s)\omega^s\big|\sqrt{f(X,X')}, \tag{D.3.8}$$

where

$$f(X,X') = \Big(\frac{\sin X}{X}\Big)^2 + \Big(\frac{\sin X'}{X'}\Big)^2 + 2\frac{\sin X}{X}\frac{\sin X'}{X'}\cos(X - X'), \tag{D.3.9}$$

and

$$X = \frac{\omega^s L}{4V_s}\big(\cos\theta - \frac{V_s}{V_r}\big) \quad \text{and} \quad X' = \frac{\omega^s L}{4V_s}\big(\cos\theta + \frac{V_s}{V_r}\big). \tag{D.3.10}$$

Figure D.2 shows for typical values, relevant for the Zeerijp tremor, the modification of the displacement spectra by Eqs. (D.3.7) and (D.3.8). The lower angular corner frequency of the S wave ω_c^s varies with θ as

$$\omega_c^s = \frac{2V_s}{L}\frac{\big[(V_s/V_r)^2 + \cos^2\theta\big]^{1/2}}{(V_s/V_r)^2 - \cos^2\theta}. \tag{D.3.11}$$

---

[9] For a circular slip plane, according to Eq. (D.3.1), $R = c'V_s/\omega_c^s$ where the constant $c' \sim 2$. For $V_r = 0.9V_s$, this relation can be rewritten as $\omega_c^s \sim 2.2V_r/R$. Inserting herein $R = W/2$, we have $\omega_c^s \sim 4.4V_r/W$, which is practically the same expression as Eq. (D.3.4).

Important is that ω_c^s as a function of $\cos\theta$ is symmetric around $\cos\theta = 0$.

According to Stein and Wysession (2003), §4.6.3, Eq. 20, the breakdown stress drop $\Delta\tau$ [Pa] follows from

$$\Delta\tau \sim \frac{8}{3\pi}\frac{M_0}{WL^2}. \tag{D.3.12}$$

With W and L proportional to corner frequencies, this expression shows that the breakdown stress drop is quite sensitive to corner frequencies.

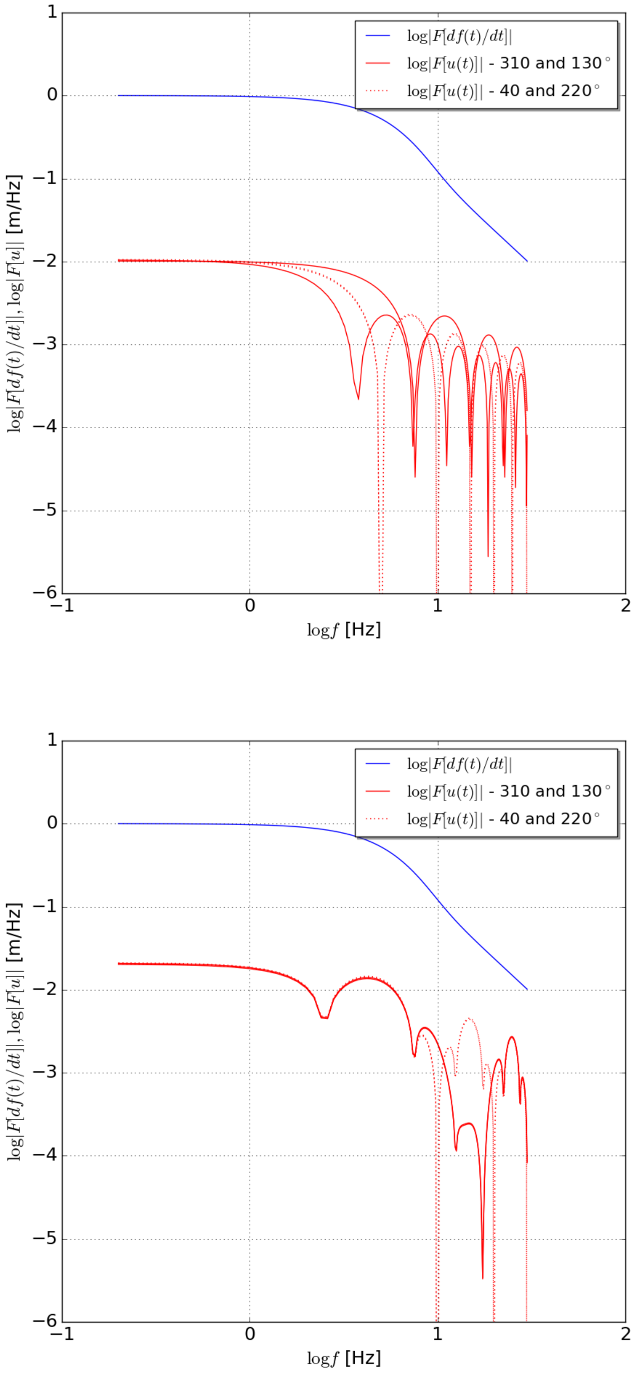

Figure D.2 : Modification of the amplitude of the displacement spectra according to Eqs. (D.3.7) and (D.3.8) for uni-directional (top figure) and bi-directional (bottom figure) rupture propagation along fault strike for four source-receiver azimuth angles.
The shape parameters of the source time function for the slip patches are $n = 2$, $t_{onset} = 5$ ms and $\tau_r = 0.08$ s. The other parameters are $L = 0.2$ km, $V_{r,strike} = 1$ km/s, $V_s = 2.2$ km/s. The take-off angle $i = 49°$ corresponding with receiver at about 5 km distance from the epicentre. The fault azimuth angle $\phi = 310°$, $\phi_s = 310$, 40, 130 and 220°.